Article

Integrated structural dynamics uncover a new B_{12} photoreceptor activation mode

https://doi.org/10.1038/s41586-025-10074-2

Received: 1 August 2025

Accepted: 17 December 2025

Published online: 4 February 2026

Check for updates

Ronald Rios-Santacruz[1,13], Harshwardhan Poddar[2,13], Kevin Pounot[3,13], Derren J. Heyes[2,13], Nicolas Coquelle[1,13], Megan J. Mackintosh[4,13], Linus O. Johannissen[2], Sara Schianchi[1], Laura N. Jeffreys[2], Elke De Zitter[1], Rory Munro[1], Martin Appleby[5], Danny Axford[6], Emma V. Beale[5], Matthew J. Cliff[2], María C. Dávila-Miliani[1], Sylvain Engilberge[1], Guillaume Gotthard[5], Kyprianos Hadjidemetriou[1,11], Samantha J. O. Hardman[2], Sam Horrell[6], Jochen S. Hub[7], Kotone Ishihara[8,9], Sofia Jaho[6], Gabriel Karras[6], Machika Kataoka[8,9], Ryohei Kawakami[8,9], Thomas Mason[5], Hideo Okumura[10], Shigeki Owada[8,10], Robin L. Owen[6], Antoine Royant[1,3], Annica Saaret[2,12], Michiyo Sakuma[2], Muralidharan Shanmugam[2], Hiroshi Sugimoto[8], Kensuke Tono[8,10], Ninon Zala[1], John H. Beale[5], Takehiko Tosha[8,9], Jacques-Philippe Colletier[1], Matteo Levantino[3], Sam Hay[2], Pawel M. Kozlowski[4], David Leys[2], Nigel S. Scrutton[2], Martin Weik[1]✉ & Giorgio Schirò[1]

Photoreceptor proteins regulate fundamental biological processes such as vision, photosynthesis and circadian rhythms[1]. A large photoreceptor subfamily uses vitamin B_{12} derivatives for light sensing[2], contrasting with the well-established mode of action of these organometallic derivatives in thermally activated enzymatic reactions[3]. The exact molecular mechanism of B_{12} photoreception and how this differs from the thermal pathways remains unknown. Here we provide a detailed description of photoactivation in the prototypical B_{12} photoreceptor CarH[4,5] from nanoseconds to seconds, combining time-resolved and temperature-resolved structural and spectroscopic methods with quantum chemical calculations. Building on the crystal structures of the initial tetrameric dark and final monomeric light-activated states[5], our structural snapshots of key intermediates in the truncated B_{12}-binding domain illustrate how photocleavage of a cobalt–carbon (Co–C) bond within the B_{12} chromophore adenosylcobalamin triggers a series of structural changes that propagate throughout CarH. Breakage of the photolabile Co–C5′ bond leads to the formation of a previously unknown adduct that links the C4′ position of the adenosyl moiety to the Co ion and can subsequently be cleaved thermally over longer timescales to allow release of the adenosyl group, ultimately causing tetramer dissociation[4,5]. This adduct, which differentiates CarH from thermally activated B_{12} enzymes, steers the photoactivation pathway and acts as the molecular bridge between photochemical and photobiological timescales. The biological relevance of our study is corroborated by kinetic data on full-length CarH in the presence of DNA. Our results offer a spatiotemporal understanding of CarH photoactivation and pave the way for designing B_{12}-dependent photoreceptors for optogenetic applications.

Photoreceptor proteins absorb light to elicit a biological response, controlling processes such as vision, circadian rhythms and plant development. Several photoreceptor families have been identified, harbouring a range of chromophores (for example, retinal, flavin adenine dinucleotide, bilin, p-coumaric acid and ketocarotenoids)[1]. How the initial photochemical events at the chromophore translate into the desired biological outcome is a current focus of intense research[6]. In particular, it is unclear how photoreceptors follow a specific reaction pathway over timescales spanning several orders of magnitude and prevent premature energy dissipation[7]. Recently, a new family of photoreceptors has been discovered that repurposes vitamin B_{12}, an organometallic enzyme cofactor known to be involved in crucial biological processes in humans and other organisms[8], for light sensing[2]. This family is estimated to include several thousand members[9,10]

---

[1]University of Grenoble Alpes, CEA, CNRS, Institut de Biologie Structurale, Grenoble, France. [2]Manchester Institute of Biotechnology, Department of Chemistry, University of Manchester, Manchester, UK. [3]ESRF — The European Synchrotron, Grenoble Cedex, France. [4]Department of Chemistry, University of Louisville, Louisville, KY, USA. [5]Paul Scherrer Institute, Villigen, Switzerland. [6]Diamond Light Source, Harwell Science and Innovation Campus, Didcot, UK. [7]Theoretical Physics and Center for Biophysics, Saarland University, PharmaScienceHub (PSH), Saarbrücken, Germany. [8]RIKEN SPring-8 Center, Hyogo, Japan. [9]University of Hyogo, Hyogo, Japan. [10]Japan Synchrotron Radiation Research Institute, Hyogo, Japan. [11]Present address: Diamond Light Source, Harwell Science and Innovation Campus, Didcot, UK. [12]Present address: Department of Biochemistry and Biophysics, Stockholm University, Stockholm, Sweden. [13]These authors contributed equally: Ronald Rios-Santacruz, Harshwardhan Poddar, Kevin Pounot, Derren J. Heyes, Nicolas Coquelle, Megan J. Mackintosh. ✉e-mail: weik@ibs.fr

and is sensitive to the green (or blue) light region of the visible spectrum. Their photoresponse can be extended to the red region either naturally in photocobilins, a recently discovered subfamily that uses red-light-absorbing linear tetrapyrrole biliverdin in close proximity to the B_{12} cofactor[11] or artificially[12,13]. B_{12}-dependent photoreceptors have become an exciting target for a number of light-dependent biotechnological and optogenetic applications, such as in the formation of light-responsive hydrogels for drug delivery, light-activated technology devices and the regulation of mammalian gene expression[14–19]. A detailed spatiotemporal description of the photoresponse in B_{12} photoreceptors is, therefore, of fundamental and applied interest.

CarH from *Thermus thermophilus* (*Tt*CarH) is a model B_{12} photoreceptor, regulating carotenoid gene expression to mitigate photooxidative stress under light exposure[4]. Previous structural work on *Tt*CarH has revealed how the B_{12} derivative adenosylcobalamin (AdoCbl; Extended Data Fig. 1a) binds at the interface of a Rossmann fold and a four-helix bundle domain (Extended Data Fig. 1b), together forming the cobalamin (Cbl)-binding domain (*Tt*CBD). Chromophore binding forces each *Tt*CBD into an extended conformation, leading to tetramerization of the *Tt*CarH[5] (Extended Data Fig. 1c). Crystal structures of the tetrameric complex bound to DNA obtained under dark conditions show how the protein interacts with DNA via flexible N-terminal DNA-binding domains to suppress gene transcription[5]. Illumination with green (or blue) light cleaves the photolabile Co–C5′ bond connecting the adenosyl (Ado) and Cbl moieties of AdoCbl and leads to the release of the final photoproduct 4′,5′-anhydroadenosine[20] by an, as yet, unknown mechanism[21]. The ensuing O_2-dependent Co redox state change is accompanied by the displacement of the Cbl corrin ring that drives a protein ligand switch[5,22] and culminates in the formation of the light-adapted state, a stable bis-histidine Cbl adduct[5] (Extended Data Fig. 1c). Large-scale reorganization of the Rossmann-fold and four-helix bundle domains is required to achieve this bis-histidine light-adapted state[5], which results in tetramer dissociation and DNA release, thereby enabling transcription[4].

What distinguishes CarH from the thermally activated B_{12} enzymes, allowing it to harness the inherent photochemical properties of the B_{12} chromophore, remains unknown. It is also unclear what the structural and chemical changes are that connect the initial dark state with the final light-adapted state. Here we used an integrated experimental and computational approach to study these light-induced changes spanning over nine orders of magnitude in time, from nanoseconds to seconds. We show that homolytic cleavage of the Co–C5′ bond leads to formation of a previously unknown Co–C4′ adduct, followed by downstream, slower structural changes that result in tetramer dissociation. By revealing the structural changes connecting photochemical and photobiological events, our results on CarH yield a holistic spatiotemporal understanding of B_{12} photoreceptor activation.

Integrated experimental and computational approach

To identify the structural and chemical changes following photon absorption and formation of the light-adapted state, we combined time-resolved and temperature-resolved structural and spectroscopic methods with quantum chemical calculations. We studied the tetrameric *Tt*CBD, which is a truncated form of *Tt*CarH lacking its N-terminal DNA-binding domains. Time-resolved UV–Vis absorption spectral changes, monitored following nanosecond excitation with green light (530 nm) of *Tt*CBD in solution (Extended Data Fig. 2 and Supplementary Note 1), revealed similar kinetics to those reported for full-length *Tt*CarH[23], validating the use of *Tt*CBD as our model.

Formation of the light-adapted state occurs via a series of spectroscopically distinct intermediates formed with respective time constants of less than 10 ns (refs. 23,24), approximately 500 ns (ref. 23), 7 ms and 600 ms (Extended Data Fig. 2 and Supplementary Note 1). UV–Vis spectral changes on the nanosecond to millisecond timescale of crystalline samples are not impacted by crystal packing (Supplementary Fig. 1). Furthermore, liquid chromatography–mass spectrometry (LC–MS) and nuclear magnetic resonance (NMR) spectroscopy demonstrate that an identical final 4′,5′-anhydroadenosine photoproduct is formed in crystallo and in solution[20] upon illumination (Supplementary Fig. 2).

To capture light-induced structural changes, time-resolved serial femtosecond crystallography (TR-SFX) experiments[25,26] were carried out on the nanosecond to millisecond timescale at the SPring-8 Angstrom compact free electron laser (SACLA)[27] and SwissFEL[28] X-ray free electron lasers (XFELs) using *Tt*CBD microcrystals (Supplementary Fig. 3). Guided by the spectroscopic kinetics, TR-SFX experiments were carried out according to an optical-laser pump–X-ray probe scheme at 10 ns, 300 ns, 3 µs, 100 µs and 3 ms (SACLA) and 3 µs and 10 ms (SwissFEL). The fluence (30 mJ cm^{-2}) of the nanosecond pump laser pulses (530 nm) was chosen based on crystallographic and spectroscopic power titrations (Extended Data Figs. 3 and 4 and Supplementary Note 2) so as to maximize the photo-converted fraction while limiting the risk of non-linear effects[29].

Structural changes were visualized in Fourier difference maps calculated between light and dark (no laser) datasets (Extended Data Fig. 5, Supplementary Figs. 4 and 5, Supplementary Video 1 and Supplementary Note 3). Intermediate-state structures were determined following structure factor amplitude extrapolation (Supplementary Video 2 and Supplementary Note 3) and were used as a basis for quantum mechanics/molecular mechanics (QM/MM) simulations to determine the likely corresponding chemical species. Density functional theory (DFT) cluster models were used to explore the chemical transformations between the Cbl species along the reaction profile. Cryogenic UV–Vis absorption measurements in vitrified solution (Extended Data Fig. 6) guided crystallography experiments on macrocrystals at the European Synchrotron Radiation Facility (ESRF) that allowed cryo-trapping of an intermediate-state structurally similar to that captured by TR-SFX at 3 µs (Supplementary Figs. 6 and 7), and whose Co redox state was assessed by cryo-trapping electron paramagnetic resonance (EPR) spectroscopy in solution (Supplementary Fig. 8). To corroborate the biological relevance of the intermediates captured by TR-SFX and inform on large-scale structural changes leading up to tetramer dissociation, time-resolved X-ray solution scattering (TR-XSS) experiments[30] were carried out on the microsecond-to-second timescale according to an optical-laser pump (532 nm)–X-ray probe scheme at the ESRF. TR-XSS experiments were also performed on full-length CarH and in the presence of DNA. Our integrated experimental and computational approach yields a holistic understanding of the CarH photoreaction mechanism across a hierarchy of timescales, revealing how fast photochemical changes drive protein structural changes via a unique rearrangement of the Ado group leading to the biological output (Fig. 1).

Diradical formation after Co–C5′ bond photolysis

In the earliest photointermediate captured by TR-SFX (10 ns, Fig. 1,ii), the Co–C5′ bond is broken as evidenced in a Fourier difference electron density map ($F_o^{\mathrm{10ns\_30mJ/cm2\_SACLA}} - F_o^{\mathrm{dark\_ref\_SACLA}}$; Fig. 2a) calculated at 2.3 Å resolution and in the 10-ns intermediate-state structure (Fig. 2b, orange model; Co–C5′ distance of 4.5 ± 0.1 Å in monomer B). Further structural changes in the active site with respect to the dark-state structure (Fig. 2b) include a shift in the W131 side chain and a tilt in the ribose moiety of the Ado group with its O3′ atom shifting by 1.7 ± 0.1 Å. Further structural changes can be identified from a distance difference matrix calculated between the 10-ns intermediate-state model (10ns_30mJ/cm2_SACLA) and the dark-state structure (dark_ref_SACLA; Fig. 2d). This reveals that part of the four-helix bundle moves away from part of the Rossmann-fold domain in a clamshell-like motion (Figs. 1d and 2d, inset); a structural change that persists at all TR-SFX time delays up to 3 ms (Extended Data Fig. 7). Our TR-SFX data indicates that the Co–C5′ bond is cleaved on a timescale faster than 10 ns, which contradicts the suggestion by Miller et al.[24] that this process occurs on a microsecond timescale simultaneously with electronically excited triplet-state decay.

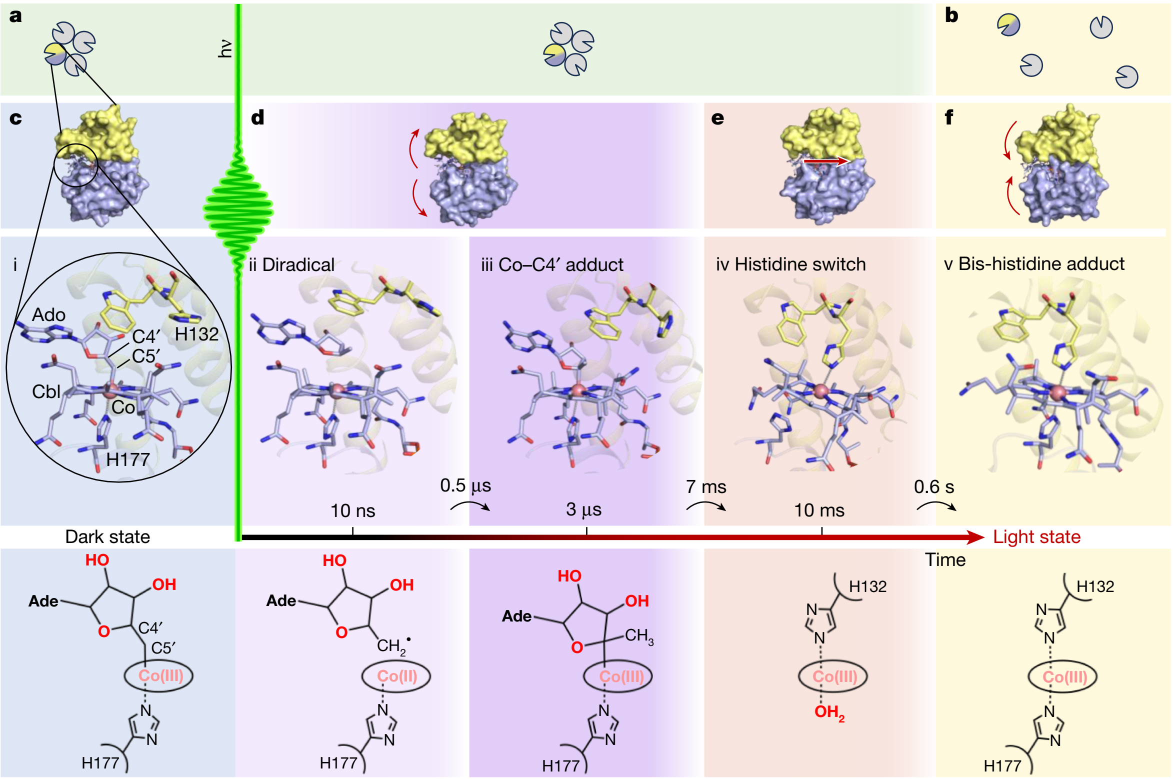

Fig. 1 | Spatiotemporal photoactivation mechanism of *Tt*CarH based on integrated application of structural, spectroscopic and computational methods. a–f, In the tetrameric dark state of *Tt*CBD (**a**), each monomer comprising a Rossmann-fold (light blue) and a four-helix bundle (yellow) domain (**c**) binds an AdoCbl chromophore with the Ado moiety linked to the Co atom within the Cbl corrin ring through its C5′ atom (i; PDB code 9S06). Following green laser photoexcitation, sequential photointermediates (ii–iv) are transiently populated to yield the monomeric (**b**) bis-histidine light-adapted state (v; PDB code 5C8F)[5]. These include a diradical state with a photocleaved Co–C5′ bond at 10 ns (ii; PDB code 9S08), a Co–C4′ adduct at 3 µs (iii; PDB code 9S0E) and mono-histidine state at 10 ms (iv; PDB code 9S0J) in which Co coordination switched from H177 to H132. Time constants (0.5 µs, 7 ms and 0.6 s) for the transitions between species ii–v are indicated. Monomer B is featured in i–v (only monomer B is considered hereafter; see Supplementary Note 3 for other monomers). Chemical schemes of species i–v are displayed in the lowest row, with Ade being the adenine moiety of Ado. Quaternary (**a**,**b**) and tertiary (**c**–**f**) structural changes, emanating from active site changes, feature clamshell-like opening (**d**), corrin ring shifting (**e**) and clamshell-like closing (**f**) associated with tetramer dissociation (**b**). Co-coordination bonds are represented by dashed lines.

We investigated the chemical nature of the 10-ns intermediate-state structure using QM/MM methods, following the same protocol as described previously[31]. A model corresponding to a diradical species with a Co(II)/C5′• radical pair (Fig. 2c) was more consistent with the experimental 10-ns intermediate-state structure (Fig. 2b, orange model) than a photoproduct model (hydridocobalamin and 4′,5′-anhydroadenosine; Supplementary Note 6), as judged from key distances, that is, Co–C5′, Co–C4′ and Co–H177NE2 (Supplementary Table 1). Therefore, we assigned the experimental 10-ns intermediate-state structure to a diradical, indicating that Co–C5′ bond photolysis is homolytic in nature, as proposed earlier[20,24].

Formation of an unexpected Co–C4′ adduct

Following Co–C5′ bond breakage, the next intermediate in the photoactivation process is formed with a spectroscopic time constant of approximately 500 ns (Fig. 1,iii and Extended Data Fig. 2a,b). This intermediate is characterized by further structural changes as evidenced by TR-SFX experiments with a 3-µs time delay between pump and probe pulses (Fig. 1,iii). The Fourier difference electron density map ($F_o^{3\mu s\_30mJ/cm2\_SACLA} - F_o^{dark\_ref\_SACLA}$; Fig. 3a, calculated at 2.25 Å resolution) and the 3-µs intermediate-state structure (Fig. 3b, orange model) indicate re-binding of the Ado group to the Co, surprisingly via the C4′ atom (Co–C4′ distance of 2.2 ± 0.1 Å, monomer B). This experimentally determined structure was optimized in a QM/MM approach according to different chemical species (Extended Data Fig. 8 and Supplementary Note 6), among which a covalent Co–C4′ adduct (Fig. 3d) whose Co–C4′ distance of 2.1 Å matches the experimentally determined value (Supplementary Table 2). Furthermore, in the QM/MM-optimized adduct (Fig. 3d), there was a 0.6 Å elongation of the Co–H177NE2 distance, which aligns with the 3-µs intermediate-state structure (2.9 and 2.6 ± 0.1 Å, respectively, compared with 2.3 ± 0.1 Å in the dark-adapted monomer B). The experimental 3-µs intermediate state is thus likely to represent a covalent Co–C4′ adduct. Before the TR-SFX experiments, a comparable Co–C4′ adduct was identified in a *Tt*CBD(H132A) mutant by serial synchrotron crystallography after laser excitation at the Diamond Light Source (Supplementary Note 4).

A structure similar to the 3-µs intermediate-state structure was obtained by temperature-controlled synchrotron cryo-crystallography[32,33] (see quantitative comparison in Supplementary Note 5). A *Tt*CBD macrocrystal was illuminated at 180 K until no more spectral changes could be observed by microspectrophotometry[34] (6 min; Supplementary Fig. 6). The crystal was then cooled to 100 K and X-ray diffraction data were collected (Fig. 3c). The similarity between the UV–Vis difference absorption spectra measured on *Tt*CBD in solution 3 µs after pump laser excitation and during steady-state illumination of a crystal at 180 K (Fig. 3e) suggests that the same reaction intermediate is formed at 3 µs and 180 K. Therefore, the redox state of the Co atom of the 3-µs intermediate-state structure can be inferred by cryo-trapping EPR measurements. EPR spectra of a flash-cooled *Tt*CBD solution following illumination at 180 K reveal that no Co(II) species are present at this stage of the reaction (Fig. 3f). As the UV–Vis absorbance

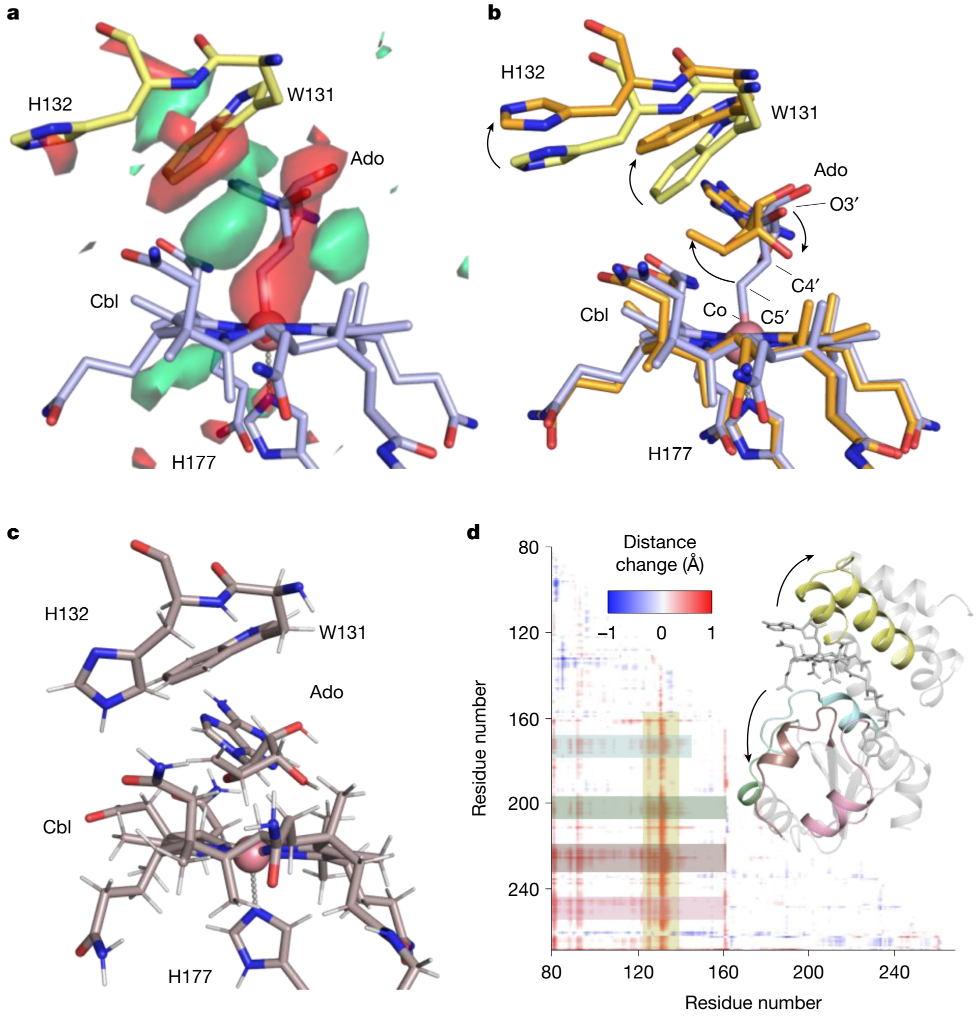

Fig. 2 | Co–C5′ bond photolysis leads to diradical formation. a, TR-SFX demonstrates Co–C5′ bond photolysis having occurred 10 ns after photon absorption as evidenced in a Fourier difference electron density map ($F_{\mathrm{o}}^{\mathrm{10ns\_30mJ/cm2\_SACLA}} - F_{\mathrm{o}}^{\mathrm{dark\_ref\_SACLA}}$) of monomer B, computed between data collected 10 ns after pump laser (530 nm) excitation and without excitation, respectively, contoured at -3.5σ (red) and $+3.5\sigma$ (green) and displayed for the AdoCbl-binding pocket. The dark-state structure (dark_ref_SACLA) is superimposed in yellow (W131 and H132) and blue (AdoCbl and H177) sticks. The map drawn over the entire tetramer is shown in Extended Data Fig. 5 and Supplementary Video 1. **b**, Overlay of the dark-state structure (dark_ref_SACLA) and the 10-ns intermediate-state structure (10ns_30mJ/cm2_SACLA) refined against extrapolated structure factor amplitudes (monomer B). The dark-state structure is coloured as in **a**, whereas the 10-ns intermediate-state structure is represented in orange sticks. The Co–C5′ distance increases from 2.0 ± 0.1 Å in the dark-state structure to 4.5 ± 0.1 Å in the 10-ns intermediate-state structure (errors estimated by the bootstrap technique; Supplementary Methods). **c**, Singlet diradical structure, based on the 10-ns intermediate-state structure and optimized by QM/MM. **d**, Distance difference matrix calculated between the Cα atoms of the 10-ns intermediate-state and the dark-state structures of monomer B. The red and blue pixels indicate intra-monomer distances becoming larger and shorter in the 10-ns intermediate-state than in the dark-state structure, respectively. The distance difference matrix information content is transcribed structurally in the inset, with the distances between part of the four-helix bundle (residues L121 to T146 in yellow) and part of the helices in the Rossmann fold domain (T171 to L183 in light blue; P200 to D206 in light green; A223 to D234 in brown; and Q249 to E262 in light magenta) increasing in the 10-ns intermediate-state structure, representing a clamshell-like movement illustrated by curved arrows in Fig. 1d. Co-coordination bonds are represented by dashed lines.

features (Fig. 3e, red) do not match those of a Co(I) species[22], it is most likely that the intermediate state present at 180 K and at 3 μs represents a Co(III)–C4′ adduct.

To the best of our knowledge, the Co–C4′ adduct has not been observed previously in B_{12}-dependent systems. Hence, the ability of CarH to form the Co–C4′ ligated species distinguishes it from thermally activated B_{12} enzymes and is linked to its unique ability to harness the inherent photoreactivity of AdoCbl. Our DFT cluster calculations (Supplementary Note 6) suggest that, after photochemical dissociation, formation of the Co–C4′ adduct is kinetically favoured over a return to the dark state (the highest barriers are approximately 5 and 14 kcal mol^{-1}, respectively; energies and structural parameters are shown in Supplementary Table 3). The DFT calculations show a substantially lower bond dissociation energy in the Co–C4′ adduct (17 kcal mol^{-1} versus 35 kcal mol^{-1} in the Co–C5′ adduct), which suggests that Co–C4′ bond breakage may occur thermally (Supplementary Fig. 9). This is not surprising as breaking the Co–C5′ bond forms a primary radical, whereas breaking the Co–C4′ bond forms a tertiary radical. Together, these data illustrate how the formation of the Co–C4′ adduct may protect the system from returning to the dark state before the Ado group has been able to escape the binding pocket. This proposed mechanism, along with a computed potential energy profile, is shown in Supplementary Fig. 9.

Ado exit, corrin ring shift and Co ligation switch

The putative Co–C4′ adduct species decays into a new intermediate state with a spectroscopic time constant of approximately 7 ms (Extended Data Fig. 2c,d), in an O_2-dependent process[22].

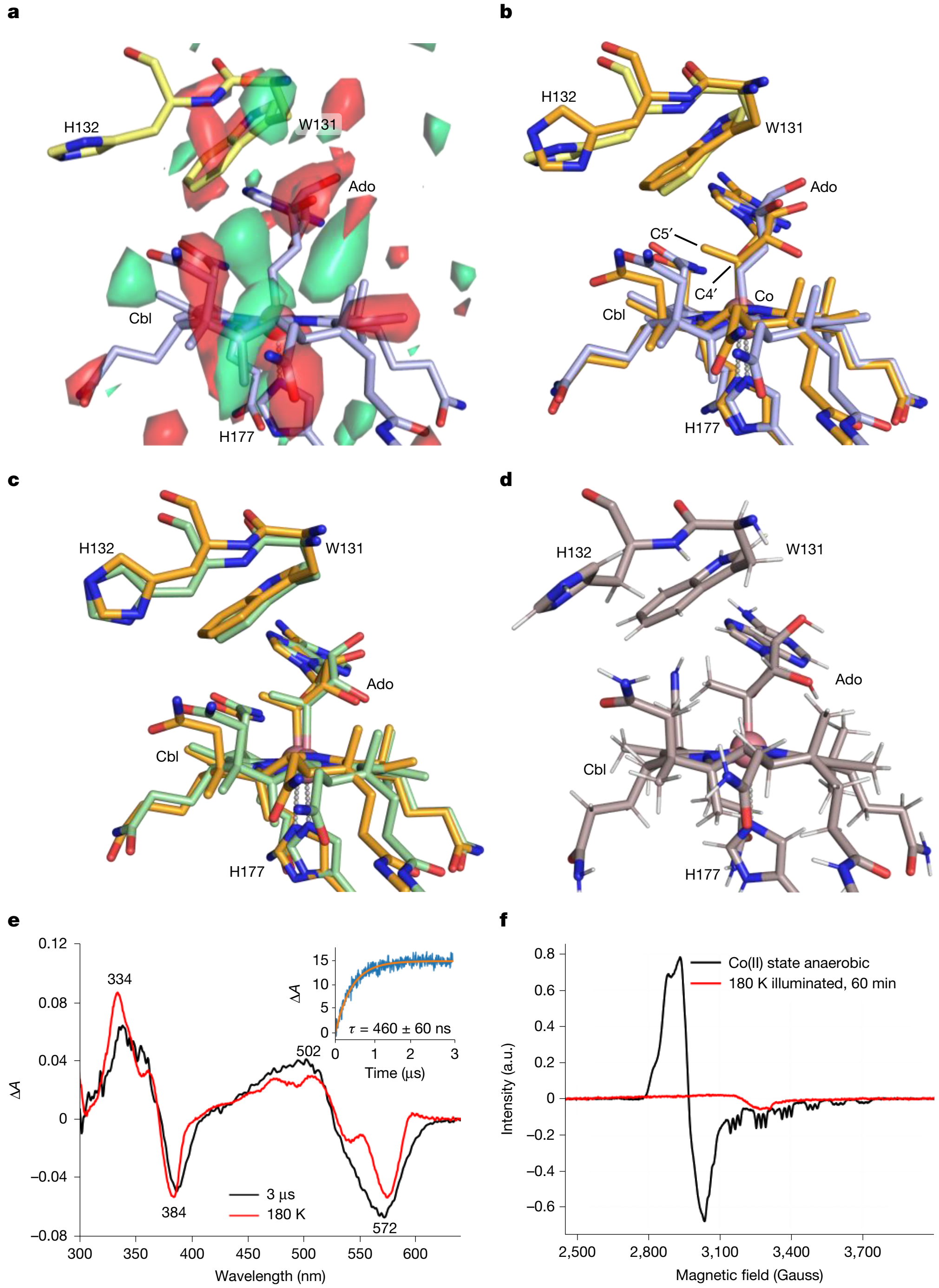

Fig. 3 | Co–C4′ adduct formed transiently. a,**b**, Structural changes in the AdoCbl-binding pocket having occurred 3 µs after photon absorption as observed by TR-SFX. **a**, The Fourier difference electron density map ($F_{\mathrm{o}}^{\mathrm{3\mu s\_30mJ/cm2\_SACLA}} - F_{\mathrm{o}}^{\mathrm{dark\_ref\_SACLA}}$) of monomer B, computed between data collected 3 µs after pump laser (530 nm) excitation and without excitation, respectively, contoured at −3.5*σ* (red) and +3.5*σ* (green) and displayed for the AdoCbl-binding pocket. The dark-state structure (dark_ref_SACLA) is superimposed in yellow (W131 and H132) and blue (AdoCbl and H177) sticks. The map drawn over the entire tetramer is shown in Extended Data Fig. 5. **b**, Overlay of the dark-state structure (dark_ref_SACLA) and the 3-µs intermediate-state structure (3µs_30mJ/cm2_SACLA) refined against extrapolated structure factor amplitudes (monomer B). The dark-state structure is coloured as in **a**, whereas the 3-µs intermediate-state structure is represented in orange sticks. **c**, Comparison of structural models obtained by cryo-trapping *Tt*CBD crystals after illumination at 180 K (green) and by TR-SFX 3 µs after photon absorption (orange). **d**, Co–C4′ adduct structure, based on the 3-µs intermediate-state structure and optimized by QM/MM. **e**, Time-resolved and temperature-resolved difference absorption spectra of *Tt*CBD in solution (50 µM). The black lines denotes the spectrum measured 3 µs after pump laser (530 nm) excitation. The red shows the spectrum measured at 77 K after illumination (530-nm LED, 15 mins) at 180 K. The inset shows a kinetic transient at 500 nm over 3 µs upon excitation with the pump laser. Data were fitted to a single exponential equation (orange line) to obtain time constants. **f**, EPR silent spectrum of *Tt*CBD in solution recorded at 20 K, after steady-state illumination (530 nm) at 180 K (red). As a reference, the signal of a Co(II) state is shown in black. Co coordination bonds are represented by dashed lines.

Structural changes that accompany the decay of the Co–C4′ adduct have been observed on the millisecond timescale by TR-SFX at the SwissFEL (Fig. 4). At 10 ms, the Fourier difference electron density map ($F_{\mathrm{o}}^{\mathrm{10ms\_30mJ/cm2\_SwissFEL}} - F_{\mathrm{o}}^{\mathrm{dark\_ref\_SwissFEL}}$; Fig. 4a, calculated at 2.9 Å resolution) points towards extensive changes at both the Ado and the Cbl groups and at H132. Indeed, the 10-ms intermediate-state structure

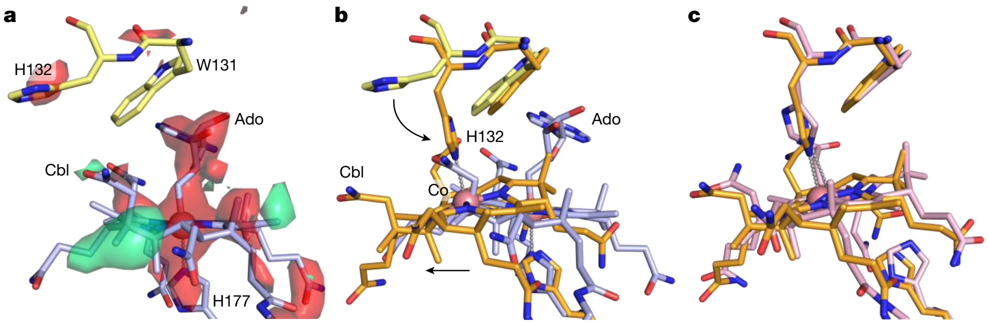

Fig. 4 | Exit of Ado moiety is followed by corrin ring displacement and Co ligation switch. **a**, Fourier difference electron density map ($F_o^{10ms\_30mJ/cm2\_SwissFEL} - F_o^{dark\_ref\_SwissFEL}$) of monomer B, computed between data collected at 10 ms after pump laser (530 nm) excitation and without excitation, respectively, contoured at −3.5*σ* (red) and +3.5*σ* (green) and displayed for the AdoCbl-binding pocket. The dark-state structure (dark_ref_SwissFEL) is shown in yellow (W131 and H132) and blue (AdoCbl and H177) sticks. The map drawn over the entire tetramer is shown in Extended Data Fig. 5. **b**, Overlay of the 10-ms intermediate-state structure (10ms_30mJ/cm2_SwissFEL; monomer B, in orange) with the dark-state structure. **c**, Overlay of the 10-ms intermediate-state structure with a synchrotron cryo-crystallography structure of *Tt*CBD (pink) obtained after illuminating a macrocrystal for 5 s at room temperature followed by flash cooling (PDB code 8C76)[22]. Co-coordination bonds are represented by dashed lines.

of monomer B, refined against extrapolated structure factor amplitudes (Fig. 4b, orange model), lacks the Ado group and features a corrin ring shifted by 4.3 ± 0.2 Å, with the Co now ligated in the upper position by H132 rather than the original, lower H177 coordination. The clamshell-like opening of the AdoCbl-binding pocket, observed between 10 ns and 3 ms (Fig. 2d), is reversed at 10 ms (Extended Data Fig. 7). The 10-ms intermediate-state structure is almost identical (root mean square deviation (r.m.s.d.) for protein Cα and Cbl atoms in monomer B of 0.6 and 1.1 Å, respectively) to the one solved by synchrotron cryo-crystallography after illuminating a *Tt*CBD macrocrystal for 5 s at room temperature followed by flash cooling[22] (Fig. 4c and Supplementary Note 3).

The same spectroscopic species forming with a time constant of approximately 7 ms has also been identified by cryogenic UV–Vis absorbance spectra collected on flash-cooled *Tt*CBD solutions illuminated at 180 K before progressive warming to higher temperatures (230–260 K) in the dark (Extended Data Fig. 6a–e). Cryogenic UV–Vis spectra (Extended Data Fig. 6f) suggest that this intermediate represents a water/OH-ligated Co(III)–H132 species (Supplementary Note 5). Hence, we conclude that the Co–C4′ adduct decays to a new state that is characterized by a shifted corrin ring structure with a Co(III) atom ligated to a single histidine residue (H132) at the upper position.

Tetramer dissociation and light-adapted state formation

Structural changes leading to the monomeric light-adapted state were measured in solution by using TR-XSS experiments covering the microsecond-to-second timescale (Fig. 5a). Data from the short time delays (100 ms or less) can be entirely reconstructed as a linear combination of only two species (Fig. 5a), with a time constant for the transition between these of 10.0 ± 0.4 ms (Fig. 5e), as revealed by a singular value decomposition (SVD) analysis[35] (Extended Data Fig. 9). The experimental 100-µs difference signal (representative of the first species) is in good agreement up to approximately 0.9 Å^{-1} (see peaks at 0.2, 0.3, 0.6 and 0.8 Å^{-1}) with the difference signals calculated using the atomic coordinates of all the TR-SFX intermediate-state structures up to 3 ms (Fig. 5d). The experimental 100-ms difference signal (representative of the second species) is in excellent agreement with the difference signal (Fig. 5c) calculated using the atomic coordinates of the corrin-ring-shifted *Tt*CBD (Protein Data Bank (PDB) code 8C76; Fig. 4c). A difference signal calculated based on a modified dark-state *Tt*CBD (8C73*), generated using the dark-state protein scaffold (PDB code 8C73) but with the Cbl atomic coordinates from the corrin-ring-shifted *Tt*CBD structure (PDB code 8C76), is also largely compatible with the 100-ms TR-XSS data (Fig. 5c). Therefore, most of the TR-XSS difference signal originates from the corrin ring shift (Fig. 4b). Figure 5c–e shows that: (1) the clamshell-like structural change revealed by SFX (Fig. 2d) occurs also in solution, without additional structural changes that would be inhibited in crystals; and (2) the clamshell-like change gives way to the corrin ring shift with a 10-ms time constant, in agreement with TR-UV–Vis kinetics (Fig. 5f, green trace).

TR-XSS data at longer time delays (more than 100 ms) were collected at a Co:dissolved O_2 ratio that allows photoreaction completion[20,22] (Supplementary Fig. 10) and reveal a new species characterized by an intense peak at approximately 0.11 Å^{-1} (Fig. 5a). These data are described by a single basis pattern (Fig. 5a) building up with a time constant of 620 ± 70 ms (Fig. 5e), as determined by SVD analysis. The near-perfect agreement between the TR-XSS signal at 3 s and the calculated signal expected for the *Tt*CBD tetramer-to-monomer transition (Fig. 5b) clearly assigns the signal change proceeding with a 620-ms time constant to the tetramer dissociation. This dissociation seems to occur in a single step (Fig. 5b and Supplementary Fig. 11). To confirm the biological relevance of the results obtained on *Tt*CBD, analogous TR-XSS data were collected on both the full-length *Tt*CarH and a *Tt*CarH–DNA complex. These datasets are in overall agreement with that on *Tt*CBD, showing comparable, albeit slightly longer, time constants (710 ± 50 and 760 ± 30 ms, respectively; Fig. 5g). The time constant for tetramer dissociation in *Tt*CBD (620 ms) is very similar to the TR-UV–Vis spectral change of 590 ± 30 ms associated with formation of the bis-histidine ligation that characterizes the light-adapted state[5] (Fig. 5f and Extended Data Fig. 2e,f). Together, we therefore assigned the build-up of the final *Tt*CBD light-adapted state (that is, bis-histidine ligated)[5] (Fig. 1,v) as concomitant with tetramer dissociation (Fig.1b).

CarH photoactivation mechanism

Our integrated experimental and computational approach combining time-resolved and temperature-resolved structural and spectroscopic methods with quantum chemical calculations provides a comprehensive picture of the photoactivated reaction in the *Tt*CBD (Fig. 1, Extended Data Fig. 10 and Supplementary Video 3). Following photon absorption by the B_{12} chromophore, the light-sensitive bond connecting the Co atom of the Cbl to the C5′ atom of the Ado group breaks homolytically, yielding a singlet diradical Co(II) species (Fig. 1,ii), the 3D structure of which was captured at 10 ns (Fig. 1,ii). The diradical species (Fig. 1,ii) is then converted on the microsecond timescale to a previously unidentified adduct between Co and the C4′ atom of the Ado group (Fig. 1,iii). The formation of the adduct is probably only possible due to the orientation of the H–C4′ bond,

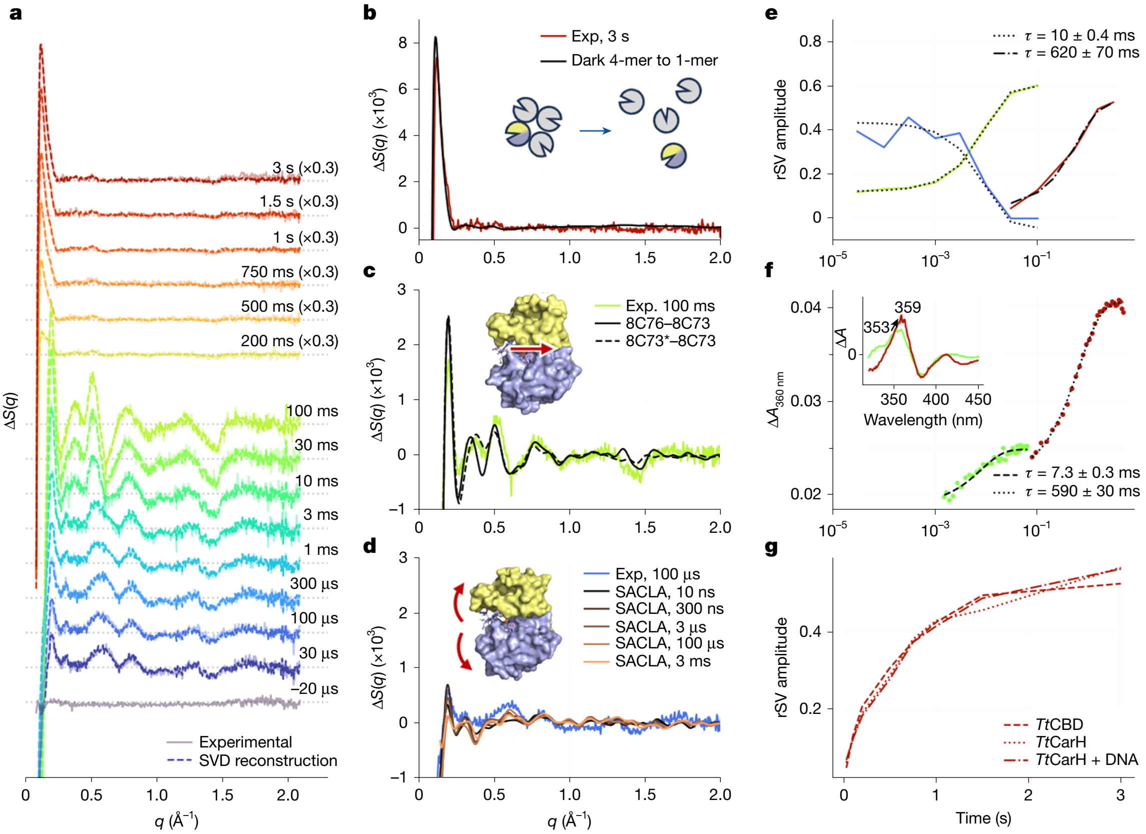

Fig. 5 | Photoinduced intermediates of *Tt*CBD in solution eventually lead to tetramer dissociation. a, TR-XSS difference signals (light–dark; Δ*S*) of the *Tt*CBD truncated construct in solution from 30 µs to 3 s (coloured continuous lines) overlaid on their SVD reconstructions (coloured dashed lines). The protein concentration in the 200 ms-to-3 s range was reduced 4× to reach a Co:dissolved O_2 ratio that enabled the photoreaction to be completed (Supplementary Methods). The signals in the 200 ms-to-3 s range are multiplied by 0.3. **b**, Comparison between the 3-s Δ*S* signal (red line) and the calculated Δ*S* signal obtained using the tetrameric dark structure (4-mer; PDB code 8C73) and a monomer (1-mer; black line). **c**, Comparison between the 100-ms Δ*S* signal (green line) and the calculated Δ*S* obtained using (1) the cryo-trapped corrin-ring-shifted structure reported previously[22] (PDB code 8C76; black continuous line), or (2) a modified tetrameric dark-state structure (8C73*) obtained using the PDB code 8C73 with the corrin ring coordinates from the cryo-trapped structure PDB code 8C76 (black dashed line). The tetrameric dark structure PDB code 8C73 was used as a reference. **d**, Comparison between the 100-µs experimental TR-XSS signal and the calculated differences obtained using TR-SFX intermediate-state structures between 10 ns and 3 ms. The tetrameric dark structure determined by SFX (PDB code 9S06) was used as a reference. **e**, Time course of the SVD right-singular vector (rSV) amplitude from the short (100 ms or less; green and blue) and the longer time-delay TR-XSS data (more than 100 ms; red). **f**, Time course of the optical absorbance change at 360 nm with (inset) the spectral differential signal at 50 ms (green continuous line) and 5 s (red continuous line). **g**, Time course of the SVD rSV amplitude from the millisecond-to-second TR-XSS datasets in *Tt*CBD, full-length *Tt*CarH and full-length *Tt*CarH complexed with DNA (*Tt*CarH–DNA).

which positions C4′ to participate in a β-H elimination reaction to form a Co adduct. This orientation seems to be specific to CarH and is not present in thermally activated B_{12} enzymes[36]. It is brought about by the positioning of the ribose group of the Ado moiety that is stabilized by a hydrogen bond between its O2′ atom and the side chain of E141. Calculated bond dissociation energies indicate that the Co–C4′ bond can be broken thermally, unlike the initial Co–C5′ bond, which requires photon absorption. We speculate that formation of the Co–C4′ adduct prevents reformation of the Co–C5′ bond that would return the diradical species to the initial dark state. The elongation of the Co–H177NE2 bond observed experimentally and computationally in the Co–C4′ adduct is consistent with a weaker bond to the upper axial ligand if one assumes that the inverse *trans* effect[37] is at play. The Co–C4′ adduct then decays on the millisecond timescale to yield an intermediate in which the Ado group has disappeared from the binding site, the corrin ring has moved by approximately 5 Å, and the Co ligation has switched from H177 to H132 (Fig. 1,iv). The associated conformational change of H132 has been suggested to cause larger-scale movements beyond the AdoCbl-binding pocket that lead to tetramer dissociation[5]. As the histidine-switched intermediate (Fig. 1,iv) does not present larger-scale movements, they are likely to occur at a later stage, presumably during reformation of the bond between Co and H177. Such larger-scale movements cannot be captured by time-resolved crystallography as the diffraction quality degrades at longer timescales, most likely because they are incompatible with crystal packing. Time-resolved X-ray solution scattering confirmed the formation of the corrin-ring-shifted intermediate in solution on the millisecond timescale and established that it is followed by tetramer-to-monomer transition occurring in a single process with a time constant of approximately 0.6 s (Fig. 1b), concomitant with formation of the final light-adapted state[5] (bis-histidine Cbl adduct; Fig. 1,v). Importantly, for the biological relevance of the results presented here, similar kinetics of monomer formation was observed in the full-length *Tt*CarH, even when bound to DNA.

The elucidated photoactivation mechanism of the *Tt*CBD spans nine orders of magnitude in time, leading from B_{12} photolysis to tetramer dissociation. Few intermediates appear to be involved, which we suggest confers robustness towards energy dissipation that would otherwise abort the photoactivation process without biological output. A Co–C4′ adduct, not observed previously in thermally activated B_{12} enzymes, is key to photoactivation, maintaining the photoreceptor on path from nanoseconds to milliseconds, thus bridging the photochemical and photobiological timescales. Formation of this crucial intermediate is facilitated by the specific orientation of the H–C4′ bond of the B_{12} cofactor with respect to the Co ion in CarH, which allows for H-atom abstraction and highlights potential routes for harnessing B_{12} photochemistry for future biotechnological innovations. The discovered intermediates and their associated reaction pathways advance our understanding of how light-driven processes in B_{12}-dependent photoreceptors differ from thermal pathways and provide crucial insights for the design and optimization of B_{12}-dependent proteins in potential optogenetics and enzyme photocatalysis applications.

Online content

Any methods, additional references, Nature Portfolio reporting summaries, source data, extended data, supplementary information, acknowledgements, peer review information; details of author contributions and competing interests; and statements of data and code availability are available at https://doi.org/10.1038/s41586-025-10074-2.

1. Kottke, T., Xie, A., Larsen, D. S. & Hoff, W. D. Photoreceptors take charge: emerging principles for light sensing. *Annu. Rev. Biophys.* **47**, 291–313 (2018).
2. Padmanabhan, S., Pérez-Castaño, R., Osete-Alcaraz, L., Polanco, M. C. & Elías-Arnanz, M. Vitamin B_{12} photoreceptors. *Vitam. Horm.* **119**, 149–184 (2022).
3. Banerjee, R. & Ragsdale, S. W. The many faces of vitamin B12: catalysis by cobalamin-dependent enzymes. *Annu. Rev. Biochem.* **72**, 209–247 (2003).
4. Ortiz-Guerrero, J. M., Polanco, M. C., Murillo, F. J., Padmanabhan, S. & Elias-Arnanz, M. Light-dependent gene regulation by a coenzyme B12-based photoreceptor. *Proc. Natl Acad. Sci. USA* **108**, 7565–7570 (2011).
5. Jost, M. et al. Structural basis for gene regulation by a B12-dependent photoreceptor. *Nature* **526**, 536–541 (2015).
6. Poddar, H. et al. A guide to time-resolved structural analysis of light-activated proteins. *FEBS J.* **289**, 576–595 (2022).
7. Miller, R. J. D., Paré-Labrosse, O., Sarracini, A. & Besaw, J. E. Three-dimensional view of ultrafast dynamics in photoexcited bacteriorhodopsin in the multiphoton regime and biological relevance. *Nat. Commun.* **11**, 1240 (2020).
8. Allen, L. H. Vitamin b-12. *Adv. Nutr.* **3**, 54–55 (2012).
9. Cheng, Z., Yamamoto, H. & Bauer, C. E. Cobalamin's (Vitamin B12) surprising function as a photoreceptor. *Trends Biochem. Sci.* **41**, 647–650 (2016).
10. Yu, Y. et al. SignatureFinder enables sequence mining to identify cobalamin-dependent photoreceptor proteins. *FEBS J.* **292**, 635–652 (2025).
11. Zhang, S. et al. Photocobilins integrate B12 and bilin photochemistry for enzyme control. *Nat. Commun.* **15**, 2740 (2024).
12. Zheng, Y., Chen, F., Frank, S., Quispe Haro, J. J. & Wegner, S. V. Three-color protein photolithography with green, red, and far-red light. *Small* **20**, 2405687 (2024).
13. Fok, H. K. F. et al. Red-shifting B12-dependent photoreceptor protein via optical coupling for inducible living materials. *Angew. Chem. Int. Ed.* **63**, e202411105 (2024).
14. Kainrath, S., Stadler, M., Reichhart, E., Distel, M. & Janovjak, H. Green-light-induced inactivation of receptor signaling using cobalamin-binding domains. *Angew. Chem. Int. Ed. Engl.* **56**, 4608–4611 (2017).
15. Chatelle, C. et al. A green-light-responsive system for the control of transgene expression in mammalian and plant cells. *ACS Synth. Biol.* **7**, 1349–1358 (2018).
16. Mansouri, M. et al. Smart-watch-programmed green-light-operated percutaneous control of therapeutic transgenes. *Nat. Commun.* **12**, 3388 (2021).
17. Wang, R., Yang, Z., Luo, J., Hsing, I. M. & Sun, F. B_{12}-dependent photoresponsive protein hydrogels for controlled stem cell/protein release. *Proc. Natl Acad. Sci. USA* **114**, 5912–5917 (2017).
18. Narayan, O. P., Mu, X., Hasturk, O. & Kaplan, D. L. Dynamically tunable light responsive silk-elastin-like proteins. *Acta Biomater.* **121**, 214–223 (2021).
19. Xu, D., Ricken, J. & Wegner, S. V. Turning cell adhesions ON or OFF with high spatiotemporal precision using the green light responsive protein CarH. *Chemistry* **26**, 9859–9863 (2020).
20. Jost, M., Simpson, J. H. & Drennan, C. L. The transcription factor CarH safeguards use of adenosylcobalamin as a light sensor by altering the photolysis products. *Biochemistry* **54**, 3231–3234 (2015).
21. Bridwell-Rabb, J. & Drennan, C. L. Vitamin B12 in the spotlight again. *Curr. Opin. Chem. Biol.* **37**, 63–70 (2017).
22. Poddar, H. et al. Redox driven B_{12}-ligand switch drives CarH photoresponse. *Nat. Commun.* **14**, 5082 (2023).
23. Kutta, R. J. et al. The photochemical mechanism of a B12-dependent photoreceptor protein. *Nat. Commun.* **6**, 7907 (2015).
24. Miller, N. A. et al. The photoactive excited state of the B12-based photoreceptor CarH. *J. Phys. Chem. B* **124**, 10732–10738 (2020).
25. Branden, G. & Neutze, R. Advances and challenges in time-resolved macromolecular crystallography. *Science* **373**, eaba0954 (2021).
26. Weik, M. & Domratcheva, T. Insight into the structural dynamics of light sensitive proteins from time-resolved crystallography and quantum chemical calculations. *Curr. Opin. Struct. Biol.* **77**, 102496 (2022).
27. Yabashi, M., Tanaka, H. & Ishikawa, T. Overview of the SACLA facility. *J. Synchrotron Radiat.* **22**, 477–484 (2015).
28. Milne, J. C. et al. SwissFEL: the Swiss X-ray free electron laser. *Appl. Sci.* **7**, 720–777 (2017).
29. Barends, T. R. M. et al. Influence of pump laser fluence on ultrafast myoglobin structural dynamics. *Nature* **626**, 905–911 (2024).
30. Pounot, K., Schiro, G. & Levantino, M. Tracking the structural dynamics of proteins with time-resolved X-ray solution scattering. *Curr. Opin. Struct. Biol.* **82**, 102661 (2023).
31. Toda, M. J., Lodowski, P., Mamun, A. A. & Kozlowski, P. M. Photoproduct formation in coenzyme B12-dependent CarH via a singlet pathway. *J. Photochem. Photobiol. B* **232**, 112471 (2022).
32. Weik, M. & Colletier, J.-P. Temperature-dependent macromolecular X-ray crystallography. *Acta Crystallogr. D* **66**, 437–446 (2010).
33. Caramello, N. & Royant, A. From femtoseconds to minutes: time-resolved macromolecular crystallography at XFELs and synchrotrons. *Acta Crystallogr. D* **80**, 60–79 (2024).
34. von Stetten, D. et al. In crystallo optical spectroscopy (icOS) as a complementary tool on the macromolecular crystallography beamlines of the ESRF. *Acta Crystallogr. D* **71**, 15–26 (2015).
35. Henry, E. R. & Hofrichter, J. in *Methods in Enzymology* (eds Brand, L. & Johnson, M. L.) Vol. 210, 129–192 (Academic Press, 1992).
36. Toda, M. J., Mamun, A. A., Lodowski, P. & Kozlowski, P. M. Why is CarH photolytically active in comparison to other B12-dependent enzymes? *J. Photochem. Photobiol. B* **209**, 111919 (2020).
37. Kuta, J., Wuerges, J., Randaccio, L. & Kozlowski, P. M. Axial bonding in alkylcobalamins: DFT analysis of the inverse versus normal trans influence. *J. Phys. Chem. A* **113**, 11604–11612 (2009).

Publisher's note Springer Nature remains neutral with regard to jurisdictional claims in published maps and institutional affiliations.

Springer Nature or its licensor (e.g. a society or other partner) holds exclusive rights to this article under a publishing agreement with the author(s) or other rightsholder(s); author self-archiving of the accepted manuscript version of this article is solely governed by the terms of such publishing agreement and applicable law.

© The Author(s), under exclusive licence to Springer Nature Limited 2026, modified publication 2026

Methods

Protein expression, purification and crystallization

The expression and purification protocols for full-length *Tt*CarH, *Tt*CBD and the variant *Tt*CBD(H132A) were adapted from those previously published for full-length *Tt*CarH[38]. Proteins with a C-terminal 6×His tag were expressed in *Escherichia coli* BL21(DE3) cells. The cells were lysed by sonication, then centrifuged and the supernatant containing the apo form of the expressed protein (that is, full-length apo-*Tt*CarH, apo-*Tt*CBD and the variant apo-*Tt*CBD(H132A)) was retained for purification. The crude extract was subjected to affinity chromatography and partially purified protein obtained after this step was incubated with AdoCbl to generate holo forms of the respective proteins in the dark. A final size-exclusion chromatography step with 50 mM Tris-HCl pH 7.5 and 100 mM NaCl as eluent was performed to achieve high purity and removal of free AdoCbl. Detailed protocols for protein expression and purification are provided in the Supplementary Methods.

For TR-SFX experiments at the SACLA and SwissFEL, macrocrystals of *Tt*CBD were produced by the batch method, at room temperature (20 °C) and under red-light conditions as recently described[22]. Those large crystals were used to generate seeds according to a recently reported protocol[39]. Microcrystals were grown by the seeded batch method using 20% PEG 10000 and 0.1 M HEPES pH 7.5. For serial synchrotron crystallography (SSX) experiments at the Diamond Light Source, *Tt*CBD(H132A) was microcrystallized in batches using a previously reported[22] crystallization condition from the LMB screen (Molecular Dimension) containing 0.1 M ammonium sulfate, 0.1 M sodium citrate pH 5.8, 16% (w/v) PEG 4000 and 20% (v/v) glycerol. For macromolecular crystallography experiments at the ESRF, macrocrystals of *Tt*CBD were obtained using a previously reported protocol[22]. Detailed crystallization procedures are provided in the Supplementary Methods.

Time-resolved absorption spectroscopy

Time-resolved absorption spectroscopy experiments after laser photoexcitation were carried out on *Tt*CBD samples in solution using an LP980-KS flash photolysis instrument (Edinburgh Instruments). Photoactivation was initiated by nanosecond laser excitation at 530 nm, using an optical parametric oscillator of a Q-switched Nd-YAG laser (NT432, EKSPLA) in a 1-cm pathlength cuvette. Laser pulses were between 6 and 8 ns in duration and varied in energy up to 20 mJ by using an attenuator. Difference absorbance spectra were recorded between 300 and 700 nm at selected time points using an image intensified CCD camera (Andor Technologies). Single-wavelength kinetic absorption transients were recorded at a range of wavelengths between 300 and 700 nm with the detection system (comprising probe light, sample, monochromator and photomultiplier) at right angles to the incident laser beam. Single-wavelength kinetic absorption transients were also collected on *Tt*CBD microcrystals embedded in sodium carboxymethyl cellulose (CMC; Sigma) in a 1-mm pathlength cuvette at a 45° angle to the incident laser beam and the probe beam. An extended version of time-resolved absorption spectroscopy methods is provided in the Supplementary Methods.

Temperature-resolved absorption spectroscopy

Static absorbance spectra were measured using a Cary 50 spectrophotometer (Agilent Technologies). For temperature-resolved absorption spectroscopy measurements, *Tt*CBD samples were cooled down to 77 K at a rate of approximately 10 K per minute in an Optistat DN liquid nitrogen cryostat (Oxford Instruments) to record spectra. Samples were then warmed to the desired temperature at a rate of 10 K per minute to initiate the reaction by illumination (1,000 µmol m^{-2} s^{-1}) with a 530-nm LED (Thorlabs) for 15 min, before cooling again to 77 K to record spectra. Room temperature absorbance spectra were also collected on *Tt*CBD microcrystals embedded in a sodium CMC matrix in a 1-mm pathlength cuvette. An extended version of temperature-resolved absorption spectroscopy methods in provided in the Supplementary Methods.

Photoproduct formation in illuminated *Tt*CBD crystals

*Tt*CBD microcrystals to be used for LC–MS and for NMR determination were either kept in the dark or placed in ambient light for 30 min and subsequently resuspended in deuterated methanol (Eurisotop).

LC–MS was undertaken on an Agilent 1100 LC-MSD instrument with an Agilent 150 × 3.0 mm Poroshell 120 SB-C18 (2.7-µm pore size) reversed phase column. An in-line electrospray ionization–time-of-flight (ESI-TOF) single quadrupole mass spectrometer (Agilent Technologies) in positive-ion mode was used to determine mass-to-charge ratios (*m*/*z*).

NMR spectra were recorded on a Bruker AVIII 500 MHz spectrophotometer with $^{1}H/^{19}F/^{13}C$-^{15}N QCI-F cryoprobe equipped with *z*-gradients. Initially, all NMR spectra were recorded using the parameters described previously[11]. In brief, 1D ^{1}H NMR spectra were collected at 298 K using a 1D ^{1}H NMR method with presaturation water suppression. Extended descriptions of the LC–MS and NMR methods used are in the Supplementary Methods.

Low-temperature cw-EPR

For EPR spectroscopy, samples containing 200 µl of 250 µM *Tt*CBD were prepared under aerobic and anaerobic conditions. The aerobic and anaerobic samples were photoactivated with a Thorlabs Mounted LED (emitting at 530 nm with a nominal output power of 370 mW) at room temperature and at 180 K, respectively. Samples were measured on a Bruker EMXplus EPR spectrometer equipped with a Bruker ER 4112SHQ/X-band resonator at 20 K (measurements at higher temperatures are stated accordingly). Data processing and analysis were performed using the EasySpin toolbox (v5.2.36) for the MATLAB program package[40]. Sample preparation and illumination protocols, as well as EPR data collection and processing details are specified in the Supplementary Information.

TR-SFX data collection and processing and structure refinement

TR-SFX experiments involving nanosecond pump-laser excitation were carried out at the SACLA[27] and SwissFEL[28] using *Tt*CBD microcrystals whose size (approximately 15 × 5 × 2 μm^3 (Supplementary Fig. 3) did not exceed in any dimension the 1/e penetration depth at 530 nm (17 µm) to ensure efficient photoexcitation at low pump-laser fluences. Spectroscopic and crystallographic pump-laser power titrations were carried out to choose the appropriate fluence (Supplementary Note 2).

For data collection at the BL2-EH3 experiment station of the SACLA, *Tt*CBD microcrystals were embedded in CMC (detailed protocol in Supplementary Methods) and extruded into a helium-filled diverse application platform for hard X-ray diffraction in SACLA[41] chamber by a high-viscosity extrusion[42] injector[43]. The SFX experiments were carried out in a time-resolved mode (TR-SFX)[25] according to an optical pump–X-ray probe scheme, using XFEL pulses at a repetition rate of 30 Hz (less than 10 fs in length, nominal photon energy of 7.996 keV (full width at half-maximum (FWHM) of 42 eV), photon flux of approximately 2×10^{11} photons per pulse and pulse energy of 300 µJ at the sample position) focused to 1.6 µm (*h*) × 1.4 µm (*v*; FWHM). The pump laser (EKSPLA NT230, 530 nm, 5 ns pulse length (FWHM), circularly polarized) was aligned perpendicular to both the X-ray beam and the high-viscosity extrusion jet and focused to a Gaussian spot with a size of 105.0 (*h*) × 98.2 μm^2 (*v*; (FWHM). TR-SFX data were collected at pump-probe delays of 10 ns, 300 ns, 3 µs, 100 µs and 3 ms and at a 3.5-µJ laser-pulse energy (fluence at the Gaussian peak of 30 mJ cm^{-2}; power density at the Gaussian peak of 6 MW cm^{-2}; nominally 2.4 absorbed photons on average per chromophore). Diffraction data with (light) and without (dark) pump-laser excitation were collected in an interleaved way.

For data collection at the Cristallina experiment station[44] of the SwissFEL, *Tt*CBD microcrystals were mounted on microstructured polymer fixed targets (MISP chips[44], 30 × 30 mm^2; a detailed protocol is in the Supplementary Methods). Interleaved light–dark TR-SFX data were collected using X-ray pulses at a repetition rate of 100 Hz (25–45 fs in length, mean photon energy of 11 keV, photon flux of 1.59×10^{11} photons per pulse and pulse energy of approximately 280 μJ at the sample position) focused to 3.7 μm (h) × 4.2 μm (v; FWHM). The pump laser (EKSPLA NT230, 532 nm and 3.5-ns pulse length (FWHM)) was fibre-coupled collinear to the X-ray beam and perpendicular to the chip plane. The $1/e^{-2}$ width of the laser spot at the sample position was determined by a beam profiler (55 μm) and assumed to be the diameter of a top-hat circular beam. TR-SFX data were collected at pump-probe delays of 3 μs and 10 ms and at 0.75-μJ laser-pulse energy (30 mJ cm^{-2}; 9 MW cm^{-2}; nominally 2.5 absorbed photons on average per chromophore). A more detailed description of TR-SFX data collections at the SACLA and SwissFEL is given in Supplementary Methods.

Offline data processing was performed using CrystFEL[45] (v0.10.1 for SACLA and v0.10.2 for SwissFEL). For the dark_ref_SACLA structure refinement, the previously reported *Tt*CBD tetramer structure (PDB code 8C73)[22] was used as a search model for molecular replacement with PHASER[46]. Iterative cycles of reciprocal space refinement performed using REFMAC5[47] from the CCP4 software suite[48] were interspersed with local real-space refinements and model building using COOT[49]. The dark_ref_SwissFEL structure refinement was carried out similarly, with the refined dark_ref_SACLA model as a search model for molecular replacement. Q-weighted Fourier difference electron density maps ($F_o^{\text{light}} - F_o^{\text{dark}}$)[50] were computed, and scalar structure factor extrapolation[51] was carried out with Xtrapol8 (ref. 52) to determine the structures of intermediate states at all time delays from experiments at both the SACLA and the SwissFEL. Models of all intermediate-state structures were refined against q-weighted extrapolated structure factor amplitudes using REFMAC5 and phenix.refine[53]. Coordinate errors were estimated using the bootstrapping approach[54]. Detailed descriptions of data processing, refinement and error estimation are available in the Supplementary Methods. Data collection and refinement statistics are presented in Supplementary Tables 4–6.

SSX data collection and processing and structure refinement

SSX after laser excitation was performed on the *Tt*CBD(H132A) mutant at beamline I24 of the Diamond Light Source[55]. Microcrystals of the *Tt*CBD(H132A) mutant (approximately 15 × 8 × 5 μm^3) were mounted on a glow-discharged silicon chip (Southampton Nanofabrication Centre, University of Southampton) with aperture size of 10–12 μm (Supplementary Methods). Two datasets were collected at room temperature: (1) without optical pump (dark_DLS), and (2) according to an optical pump–X-ray probe scheme (illuminated_DLS). Using an X-ray beam of 12.4 keV focused to 8 μm (h) × 8 μm (v; FWHM), each crystal was exposed for 10 ms with a photon flux of 1.6×10^{12} photons per second and diffraction data were recorded. For the SSX data collection involving illumination, a portable pulsed laser system from Light Conversion (PORTO) was used to photoactivate the *Tt*CBD(H132A) microcrystals. Mirrors and an achromatic focusing lens were used to focus the laser beam at the sample position, in such a geometry that the laser beam was approximately 15° off-axis from the X-ray beam with a laser beam size of 50 μm (FWHM) in horizontal and vertical directions. The laser was operated at a wavelength of 515 nm and a repetition rate of 50 kHz, providing individual pulses of 300 fs. The laser intensity at the sample position was attenuated using a neutral density filter, yielding a laser power of 0.8 mW; that is, 0.016 μJ per 300-fs pulse. With this setup, pump-laser excitation was performed during 10 ms (that is, 500 pulses), corresponding to a pump-laser energy of 8 μJ, a fluence of 320 mJ cm^{-2} and to nominally 12 absorbed photons per chromophore assuming an average crystal size of 8 μm. Diffraction images were collected during 10 ms immediately after laser exposure. This dataset was collected with the pump laser on for all apertures of the chip, that is, no dark interleaved was collected.

For the dark_DLS structure refinement, molecular replacement was performed with PHASER[46] using as a search model the structure of the dark-adapted *Tt*CBD(H132A) mutant (PDB code 8C35), followed by a refinement procedure similar to the one described above for the dark_ref_SACLA structure refinement. Refinement of an illuminated_DLS model against extrapolated structure factor amplitudes was not possible, as Fourier difference maps were uninterpretable due to an unexpectedly high R_{iso} value (19.3%). Instead, composite-model refinement was performed as described in the Supplementary Methods. Data collection and refinement statistics are in Supplementary Table 7.

Macromolecular crystallography and in crystallo spectroscopy

Cryo-temperature dependent macromolecular crystallography in combination with in crystallo UV–Vis absorption microspectrophotometry[34] on the BM07-FIP2 beamline of the ESRF[56] was used to characterize structural and spectroscopic changes in crystalline *Tt*CBD after light illumination at 180 K. Details on the illumination and temperature-cycling protocols, as well as on X-ray data collection and processing and structure refinement are given in Supplementary Methods. Data collection and refinement statistics are reported in Supplementary Table 8.

TR-XSS data collection and reduction

TR-XSS data were collected at the ID09 beamline of the ESRF[57,58]. The protein solutions (*Tt*CBD, *Tt*CarH and a *Tt*CarH–DNA complex) were photoexcited with a 5-ns pulsed laser (EKSPLA NT342B) at 532 nm. The laser was focused with cylindrical lenses to an elliptical spot approximately 2.0 (h) × 0.2 mm^2 (v; FWHM) corresponding to a fluence of 50 mJ cm^{-2} and 2.5 absorbed photons per chromophore. X-rays (14.7 keV) probed the sample at 90° with respect to the laser incoming direction. Scattering patterns were recorded on a Rayonix MX170-HS and azimuthally integrated to obtain 1D scattering signals $S(q)$. TR-XSS difference signals $\Delta S(q)$ were obtained as the difference between the signals measured after photoexcitation minus the signal measured before photoexcitation. Data reduction was performed using the txs Python package developed at ID09 (https://gitlab.esrf.fr/levantin/txs).

Two different TR-XSS datasets were collected on *Tt*CBD: the first dataset (30 μs to 100 ms) was obtained by flowing a high-concentration sample through a quartz capillary in a closed loop with a peristaltic pump (Minipuls, Gilson); and the second dataset (100 ms to 3 s) was obtained by flowing a low-concentration sample through a quartz capillary with a syringe pump (Fusion 4000X, Chemyx). The lower concentration in the second dataset ensured a protein chromophore concentration approximately half of the oxygen concentration in solution, with fully aerobic conditions allowing completion of the photoreaction up to tetramer dissociation[20,22]. A protocol analogous to that used for the second dataset was also used to collect data on *Tt*CarH and a *Tt*CarH–DNA complex in the time interval of 100 ms to 3 s. An extended description of the TR-XSS methods is given in the Supplementary Methods.

Cluster model calculations

We used DFT cluster models to examine the mechanism for the formation of a Co–C4′ adduct and explore the inherent differences in the chemistry of the Co–C5′ and Co–C4′ adducts. These calculations were performed in Gaussian16 rev. D[59] using the BP86 functional[60], which has been shown to perform well for B_{12} systems[61,62], with the Def2-TZVP basis set on cobalt and the 6-31 G(d,p) basis sets on the remaining atoms, an implicit solvation model (CPCM) with dielectric constant of 5.0 and empirical dispersion (GD3BJ)[63,64]. The cluster model was constructed from the dark_DLS model of the *Tt*CBD(H132A) mutant (monomer A) and consisted of a truncated Cbl, Ado and binding-site residues W131 and H177 truncated as $-CH_3$ at the Cβ and V138, E141 and H142 truncated as CHO and NH_2 C and N termini, respectively (Supplementary Fig. 12) for a total of 211 atoms, with a net charge of 0. Six atoms were kept fixed during the calculations: the Cβ of W131 and H177, the Cα of V138, E141 and H142 and the Co. Comparison with the *Tt*CBD crystal structure (dark_ref_SACLA) revealed that the fixed atoms could be overlayed with a r.m.s.d. of 0.1 Å. The potential energy profile for the interconversion between Co–C4′ adduct, photoproduct and Co–C5′ adduct (Supplementary Fig. 9) was calculated using relaxed potential energy scans, and all transition states were fully optimized, and frequency calculations confirmed the presence of a single imaginary frequency. All calculations were performed with singlet multiplicity, as the short timescales of Co–C5′ cleavage rule out a triplet mechanism and we have not observed any triplet species by EPR. Results of cluster model calculations are presented in Supplementary Note 6.

QM/MM setup and simulation

Computational models of dark and intermediate state structures were created based on a monomer of the corresponding crystal structures (dark_ref_SACLA, 10ns_30mJ/cm^2_SACLA and 3μs_30mJ/cm^2_SACLA) and minimized using the ff14sb AMBER force field[65]. Hydrogens were added with Amber16 (ref. 66). The AMBER parameters for AdoCbl were obtained from Marques et al.[67]. In preparation for QM/MM simulations, the models were divided into a higher (QM) and a lower (MM) layer (Supplementary Fig. 13). The QM layer contained 170 atoms and comprised the Ado group of the chromophore, corrin ring (including cobalt ion and corrin side chains) and the imidazole portion of H177. The MM layer comprised the nucleotide loop of the chromophore (including the dimethylbenzimidazole), the H177 backbone atoms and all atoms of residues other than H177. The QM region was treated with DFT using the BP86 functional along with the TZVP basis set for H and the TZVPP basis set for Co, C, N and O[68–72]. Any residue that had at least one atom within 10 Å of the cobalt was kept unfrozen, meaning it was allowed to freely move throughout the course of the optimizations. The QM/MM models were optimized using Gaussian09[73].

Reporting summary

Further information on research design is available in the Nature Portfolio Reporting Summary linked to this article.

Data availability

Crystal structures have been deposited at the PDB under the accession codes: 9S0A, 9S0B, 9S0C, 9S0D, 9S0E, 9S0F, 9S0G, 9S0H, 9S0I, 9S0J, 9S06, 9S07, 9S08 and 9S09. All indexed raw images, as well as CrystFEL stream files and merged mtz files for each SFX dataset of this study have been deposited in the Coherent X-ray Imaging Data Bank (CXIDB) with accession ID 237. For all time-resolved datasets, the Fourier difference maps computed with their respective reference datasets have also been deposited (https://doi.org/10.11577/2999572). The CXIDB nomenclature for the different datasets corresponds to the nomenclature used in Supplementary Tables 4–6. The TR-XSS data (https://doi.org/10.15151/ESRF-ES-704502367 and https://doi.org/10.15151/ESRF-ES-1437867878) and the cryo-macromolecular crystallography data (https://doi.org/10.15151/ESRF-DC-2303883862) are available as raw acquisition data from the ESRF (https://www.esrf.fr).

38. Poddar, H. et al. An unusual light-sensing function for coenzyme B_{12} in bacterial transcription regulator CarH. *Methods Enzymol.* **668**, 349–372 (2022).
39. Shoeman, R. L., Hartmann, E. & Schlichting, I. Growing and making nano- and microcrystals. *Nat. Protoc.* **18**, 854–882 (2023).
40. Stoll, S. & Schweiger, A. EasySpin, a comprehensive software package for spectral simulation and analysis in EPR. *J. Magn. Reson.* **178**, 42–55 (2006).
41. Tono, K. et al. Diverse application platform for hard X-ray diffraction in SACLA (DAPHNIS): application to serial protein crystallography using an X-ray free-electron laser. *J. Synchrotron Radiat.* **22**, 532–537 (2015).
42. Botha, S. et al. Room-temperature serial crystallography at synchrotron X-ray sources using slowly flowing free-standing high-viscosity microstreams. *Acta Crystallogr. D* **71**, 387–397 (2015).
43. Shimazu, Y. et al. High-viscosity sample-injection device for serial femtosecond crystallography at atmospheric pressure. *J. Appl. Crystallogr.* **52**, 1280–1288 (2019).
44. Carrillo, M. et al. Micro-structured polymer fixed targets for serial crystallography at synchrotrons and XFELs. *IUCrJ* **10**, 678–693 (2023).
45. White, T. Processing serial crystallography data with CrystFEL: a step-by-step guide. *Acta Crystallogr. D* **75**, 219–233 (2019).
46. McCoy, A. J. et al. Phaser crystallographic software. *J. Appl. Crystallogr.* **40**, 658–674 (2007).
47. Murshudov, G. N. et al. REFMAC5 for the refinement of macromolecular crystal structures. *Acta Crystallogr. D* **67**, 355–367 (2011).
48. Agirre, J. et al. The CCP4 suite: integrative software for macromolecular crystallography. *Acta Crystallogr. D* **79**, 449–461 (2023).
49. Emsley, P., Lohkamp, B., Scott, W. G. & Cowtan, K. Features and development of Coot. *Acta Crystallogr. D* **66**, 486–501 (2010).
50. Ursby, T. & Bourgeois, D. Improved estimation of structure-factor difference amplitudesfrom poorly accurate data. *Acta Crystallogr. A* **53**, 564–575 (1997).
51. Genick, U. Structure-factor extrapolation using the scalar approximation: theory, applications and limitations. *Acta Crystallogr. D* **63**, 1029–1041 (2007).
52. De Zitter, E., Coquelle, N., Oeser, P., Barends, T. R. M. & Colletier, J. P. Xtrapol8 enables automatic elucidation of low-occupancy intermediate-states in crystallographic studies. *Commun. Biol.* **5**, 640 (2022).
53. Liebschner, D. et al. Macromolecular structure determination using X-rays, neutrons and electrons: recent developments in Phenix. *Acta Crystallogr. D* **75**, 861–877 (2019).
54. Gorel, A., Schlichting, I. & Barends, T. R. M. Discerning best practices in XFEL-based biological crystallography — standards for nonstandard experiments. *IUCrJ* **8**, 532–543 (2021).
55. Horrell, S. et al. Fixed target serial data collection at diamond light source. *J. Vis. Exp.* **168**, e62200 (2021).
56. McCarthy, A. A. et al. Current and future perspectives for structural biology at the Grenoble EPN campus: a comprehensive overview. *J. Synchrotron Radiat.* **32**, 577–594 (2025).
57. Wulff, M. et al. The realization of sub-nanosecond pump and probe experiments at the ESRF. *Faraday Discuss.* **122**, 13–26 (2003).
58. Cammarata, M. et al. Chopper system for time resolved experiments with synchrotron radiation. *Rev. Sci. Instrum.* **80**, 015101 (2009).
59. Gaussian 16 Rev. A.03 (Wallingford, CT, 2016).
60. Becke, A. D. Density-functional thermochemistry. III. The role of exact exchange. *J. Chem. Phys.* **98**, 5648–5652 (1993).
61. Kornobis, K. et al. Electronically excited states of vitamin B12: benchmark calculations including time-dependent density functional theory and correlated ab initio methods. *J. Phys. Chem. A* **115**, 1280–1292 (2011).
62. Hirao, H. Which DFT functional performs well in the calculation of methylcobalamin? Comparison of the B3LYP and BP86 functionals and evaluation of the impact of empirical dispersion correction. *J. Phys. Chem A* **115**, 9308–9313 (2011).
63. Grimme, S., Ehrlich, S. & Goerigk, L. Effect of the damping function in dispersion corrected density functional theory. *J. Comput. Chem.* **32**, 1456–1465 (2011).
64. Grimme, S., Antony, J., Ehrlich, S. & Krieg, H. A consistent and accurate ab initio parametrization of density functional dispersion correction (DFT-D) for the 94 elements H-Pu. *J. Chem. Phys.* **132**, 154104 (2010).
65. Maier, J. A. et al. ff14SB: improving the accuracy of protein side chain and backbone parameters from ff99SB. *J. Chem. Theory Comput.* **11**, 3696–3713 (2015).
66. Case, D. A. et al. AmberTools. *J. Chem. Inf. Model.* **63**, 6183–6191 (2023).
67. Marques, H. M., Ngoma, B., Egan, T. J. & Brown, K. L. Parameters for the amber force field for the molecular mechanics modeling of the cobalt corrinoids. *J. Mol. Struct.* **561**, 71–91 (2001).
68. Perdew, J. P. Density-functional approximation for the correlation energy of the inhomogeneous electron gas. *Phys. Rev. B* **33**, 8822–8824 (1986).
69. Runge, E. & Gross, E. K. U. Density-functional theory for time-dependent systems. *Phys. Rev. Lett.* **52**, 997–1000 (1984).
70. Becke, A. D. Density-functional exchange-energy approximation with correct asymptotic behavior. *Phys. Rev. A* **38**, 3098–3100 (1988).
71. Weigend, F., Häser, M., Patzelt, H. & Ahlrichs, R. RI-MP2: optimized auxiliary basis sets and demonstration of efficiency. *Chem. Phys. Lett.* **294**, 143–152 (1998).
72. Eichkorn, K., Weigend, F., Treutler, O. & Ahlrichs, R. Auxiliary basis sets for main row atoms and transition metals and their use to approximate Coulomb potentials. *Theor. Chem. Acc.* **97**, 119–124 (1997).
73. Frisch, M. J. et al. Gaussian 09, revision B.01. (2010).

Acknowledgements M.W., G.S. and J.-P.C. thank I. Schlichting, R. Shoeman, B. Doak and T. Barends for long-standing support, advice and collaboration related to all aspects of serial crystallography experiments. G.S. and M.L. are grateful to M. Cammarata for the invaluable long-term advice and collaboration and the helpful discussions on several aspects of the time-resolved X-ray solution scattering experiments. M.W. acknowledges a stimulating discussion with D. Le Bolloc'h on energy dissipation in photoreceptors. M.W., G.S. and R.R.-S. thank I. Schlichting and R. L. Shoeman and S. M. Kapetanaki for their time invested during the screening beamtimes at the LCLS (P240) and the EuXFEL (PCS proposal no. 3007), respectively. The study was supported by ANR grants to G.S. and M.L. (PhotoGene) and to M.W. (BioXFEL), by CNRS grants to G.S. (XFEL Instruments) and to M.W. (GoToXFEL), and a grant to M.W. by GRAL, a project of the University Grenoble Alpes graduate school (Ecoles Universitaires de Recherche) CBH-EUR-GS (ANR-17-EURE-0003). M.W. and T.T. acknowledge financial support from the Partenariat Hubert Curien Sakura program, jointly funded by the Ministère de l'Europe et des Affaires étrangères (MEAE) and the Ministère de l'Enseignement supérieur et de la Recherche (MESR) of France and the Japan Society for the Promotion of Science of Japan. R.M. was supported by a GRAL PhD grant to J.-P.C. We thank E. A. Andreeva for advice on viscous matrix preparation for microcrystal injection; the EPSRC for access to the National Research Facility for Electron Paramagnetic Resonance Spectroscopy (NS/A000055/1 and EP/W014521/1); and the SACLA and SwissFEL staff for assistance. Funding from an EPSRC International Centre-to-Centre grant no. EP/S030336/1 was awarded to D.J.H., D.L. and N.S.S. R.R.-S. acknowledges travel grants from the EMBO (scientific exchange grant number 9591) and the Université Grenoble Alpes for a 1-month stay at the SACLA (Research Support Program for Graduate Students). R.R.-S. and S.S. were supported by CEA CFR PhD grants to M.W. M.C.D.-M. was supported by a PhD grant from the Ecole Normale Supérieure Paris. XFEL experiments were carried out at BL2-EH3 of the SACLA with the approval of the Japan Synchrotron Radiation Research Institute (proposal no. 2022B8815), at the SwissMX instrument at the Cristallina experiment station of SwissFEL (proposal 20231018). This project has received funding from the European Union's Horizon 2020 research and innovation programme under the Marie Skłodowska-Curie grant agreement no. 884104 (PSI-FELLOW-III-3i). The SwissFEL Cristallina experimental station at the Paul Scherrer Institut was realized with financial support from the Swiss National Science Foundation and the University of Zurich under project no. 206021_183330. We acknowledge the use of the Park Innovaare Cleanroom for Optics and innovation for the production of the MISP chips. The ESRF is acknowledged for providing beamtimes (LS-3091, BLC-14546, LS-3226, LS-3303 and LS-3364) at the ID09 beamline. We acknowledge the French Biology/Health Panel Review Committee for the provision of synchrotron radiation beamtime at the ESRF on beamline BM07-FIP2, supported by the French ANR PIA3 (France 2030) EquipEx+ project MAGNIFIX under grant agreement ANR-21-ESRE-0011. We acknowledge the ESRF for the provision of beamtime for crystal screening and data collection (MX2686, MX2498 and MX2398) on beamlines ID30A-1, ID30A-3, ID23-1 and ID23-2 and the macromolecular crystallography group members for excellent support. SSX experiments were carried out at the I24 beamline at the Diamond Light Source under proposal numbers MX24447 and MX31850. The PORTO laser at Diamond was funded by the EPSRC (EP/P001548/1). This work was partially carried out at the platforms of the Grenoble Instruct-ERIC Center (IBS and ISBG; UMS 3518 CNRS-CEA-UGA-EMBL) within the Grenoble Partnership for Structural Biology. Platform access was supported by FRISBI (ANR-10-INBS-05-02) and GRAL. The IBS acknowledges integration into the Interdisciplinary Research Institute of Grenoble (IRIG, CEA). M.J.M. and P.M.K. acknowledge the Cardinal Research Cluster at the University of Louisville for access to high-performance computing resources.

Author contributions D.J.H. and G.S. conceived the project. D.J.H., M.L., N.S.S., M.W. and G.S. designed and organized the overall research. The main manuscript was written by D.J.H., M.J.M., M.W. and G.S., with input from R.R.-S., H.P., N.C., L.O.J., L.N.J., E.D.Z., K.H., S. Howell, S.J., R.L.O., J.H.B., J.-P.C., T.T., M.L., S. Hay, P.M.K., D.L. and N.S.S. The Supplementary Information was written by R.R.-S., H.P., K.P., D.J.H., N.C., M.J.M., L.O.J., S.S., L.N.J., M.L., S. Hay, P.M.K., M.W. and G.S. Protein expression and purification were carried out by R.R.-S., H.P., S.S., M.C.D.-M. and N.Z., for *Tt*CBD by H.P., and M. Sakuma for *Tt*CBD(H132A) and full-length *Tt*CarH. Microcrystals for SFX were produced by R.R.-S., S.S. and K.H., and for SSX by H.P. Macrocrystals for macromolecular crystallography were grown by R.R.-S., H.P. and S.S. Microcrystal injection conditions were established by R.R.-S. and G.S. Microcrystal diffraction quality was tested at ESRF and SPring-8 by R.R.-S., T.T. and G.S. SFX experiments at the SACLA and SwissFEL were performed by R.R.-S., H.P., D.J.H., N.C., S.S., L.N.J., E.D.Z., M.A., E.V.B., M.C.D.-M., G.G., S.J.O.H., K.I., M.K., R.K., T.M., R.M., H.O., S.O., A.S., M. Sakuma, H.S., K.T., J.H.B., J.-P.C., T.T., M.W. and G.S. SSX experiments at the Diamond Light Source were performed by H.P., D.A., S. Howell, S.J., G.K. and R.L.O. Offline data processing, analysis and structure refinement were conducted by R.R.-S., N.C., E.D.Z. and J.-P.C., by H.P. for SFX and by N.C. for SSX. Cryo-temperature-dependent macromolecular crystallography experiments were carried out by R.R.-S., H.P., D.J.H., S.S., L.N.J., M.C.D.-M., S.E., A.R., M.W. and G.S., with data analysis and structure refinement by R.R.-S., N.C. and S.S. TR-XSS experiments at the ID09/ESRF were performed by R.R.-S., H.P., K.P., D.J.H., L.N.J., M.L. and G.S., with data reduction by K.P. and M.L., and analysis and interpretation by K.P., J.S.H., M.L. and G.S. NMR spectra were collected and interpreted by L.N.J. and M.J.C. LC–MS data were collected and interpreted by L.N.J. QM/MM calculations were performed, analysed and interpreted by M.J.M. and P.M.K. DFT cluster calculations were performed, analysed and interpreted by L.O.J. and S. Hay. Time-resolved and temperature-resolved UV–Vis spectroscopy was carried out and interpreted by H.P., D.J.H. and S.J.O.H. EPR data were collected and interpreted by H.P., D.J.H. and M. Shanmugam.

Competing interests The authors declare no competing interests.

Additional information
Supplementary information The online version contains supplementary material available at https://doi.org/10.1038/s41586-025-10074-2.
Correspondence and requests for materials should be addressed to Martin Weik.
Peer review information *Nature* thanks the anonymous reviewer(s) for their contribution to the peer review of this work. Peer reviewer reports are available.
Reprints and permissions information is available at http://www.nature.com/reprints.

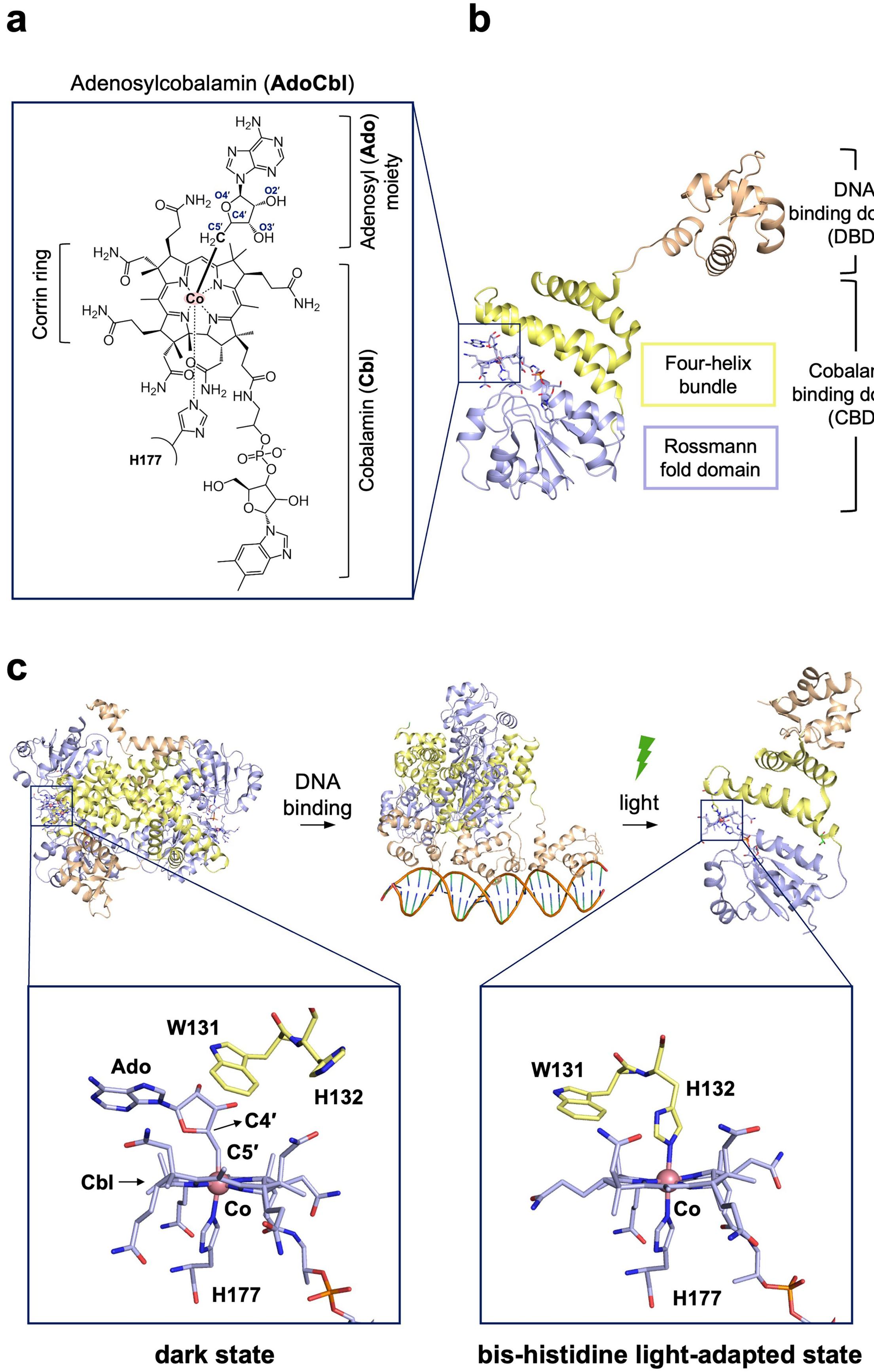

Extended Data Fig. 1 | See next page for caption.

Extended Data Fig. 1 | Crystal structures of full-length *Tt*CarH before and after illumination[5]. (**a**) Chemical structure of adenosylcobalamin (AdoCbl). The cobalt atom is shown as a pink sphere and the photolabile Co-C5′ bond depicted in bold. (**b**) The monomer of full length *Tt*CarH is composed of two domains: a DNA binding domain (DBD) and the cobalamin binding domain (CBD). The CBD consists of two motifs, a four-helix bundle and a Rossmann fold domain. (**c**) Structural changes after photoactivation of *Tt*CarH. In the upper row, models of full length *Tt*CarH in its dark state (tetrameric form) are shown in cartoon in absence of (left, PDB entry code 5C8D) and complexed (middle, PDB entry code 5C8E) to DNA. The inset (lower left) represents the AdoCbl in the dark state as well as key residues (H132, W131 and H177) in sticks. In the dark state, the cobalt atom is covalently bound (Co–C5′) to the adenosyl moiety and also coordinated to H177. Upon photoactivation, the Co–C5′ bond breaks. Thus, the adenosyl group leaves the chromophore binding pocket and structural reorganisations yield to tetramer dissociation and formation of monomers (middle row, right) bis-histidine light-adapted state (lower right, PDB entry code 5C8F).

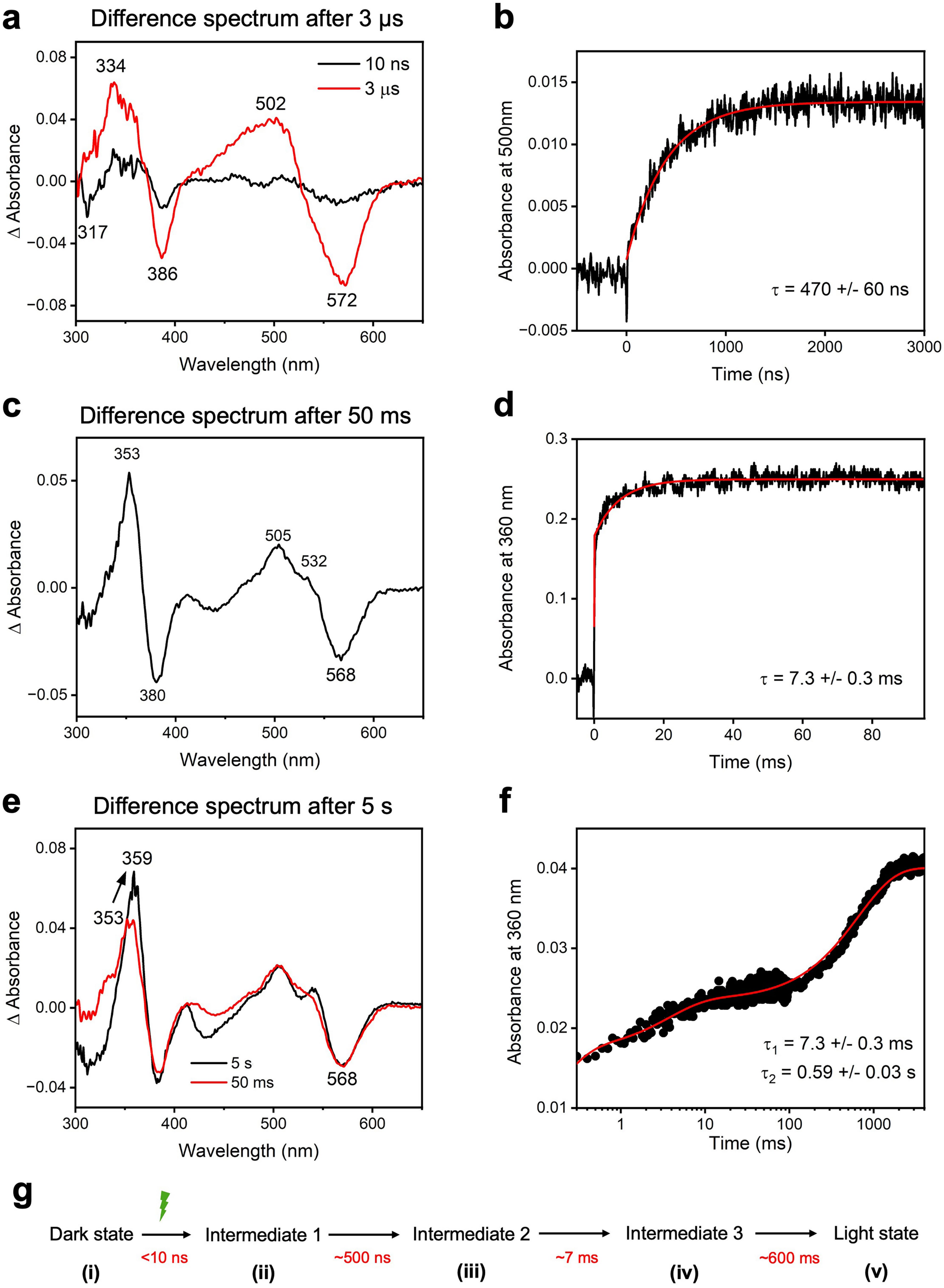

Extended Data Fig. 2 | See next page for caption.

Extended Data Fig. 2 | Formation of intermediate states in the photochemical reaction pathway of *Tt*CBD in solution monitored by TR-absorption spectroscopy after excitation at 530 nm. Time-dependent difference absorbance spectra of samples containing 50 µM *Tt*CBD are shown 10 ns, 3 µs (**a**), 50 ms (**c**) and 5 s (**e**) after excitation with a ns laser pulse at 530 nm. The wavelengths of the main spectral changes are labelled accordingly. (**b**) Kinetic transients at 500 nm on the µs timescale of samples containing 50 µM *Tt*CBD. (**d**) Kinetic transients at 360 nm on the ms timescale of samples containing 50 µM *Tt*CBD. (**f**) Kinetic transients at 360 nm on the ms-s timescale of samples containing 50 µM *Tt*CBD. Data were fitted to a mono-exponential (**b,d**) or a bi-exponential (**f**) function (red lines) to obtain time constants. All transients were measured at room temperature and data shown are the average of at least five traces. (**g**) The time-resolved absorption spectroscopy data yield the reaction scheme shown here, indicating the time constants for the formation of each of the intermediate states. The *i*, *ii*, *iii*, *iv* and *v* labels illustrate how these species relate to those depicted in Fig. 1 of the main text.

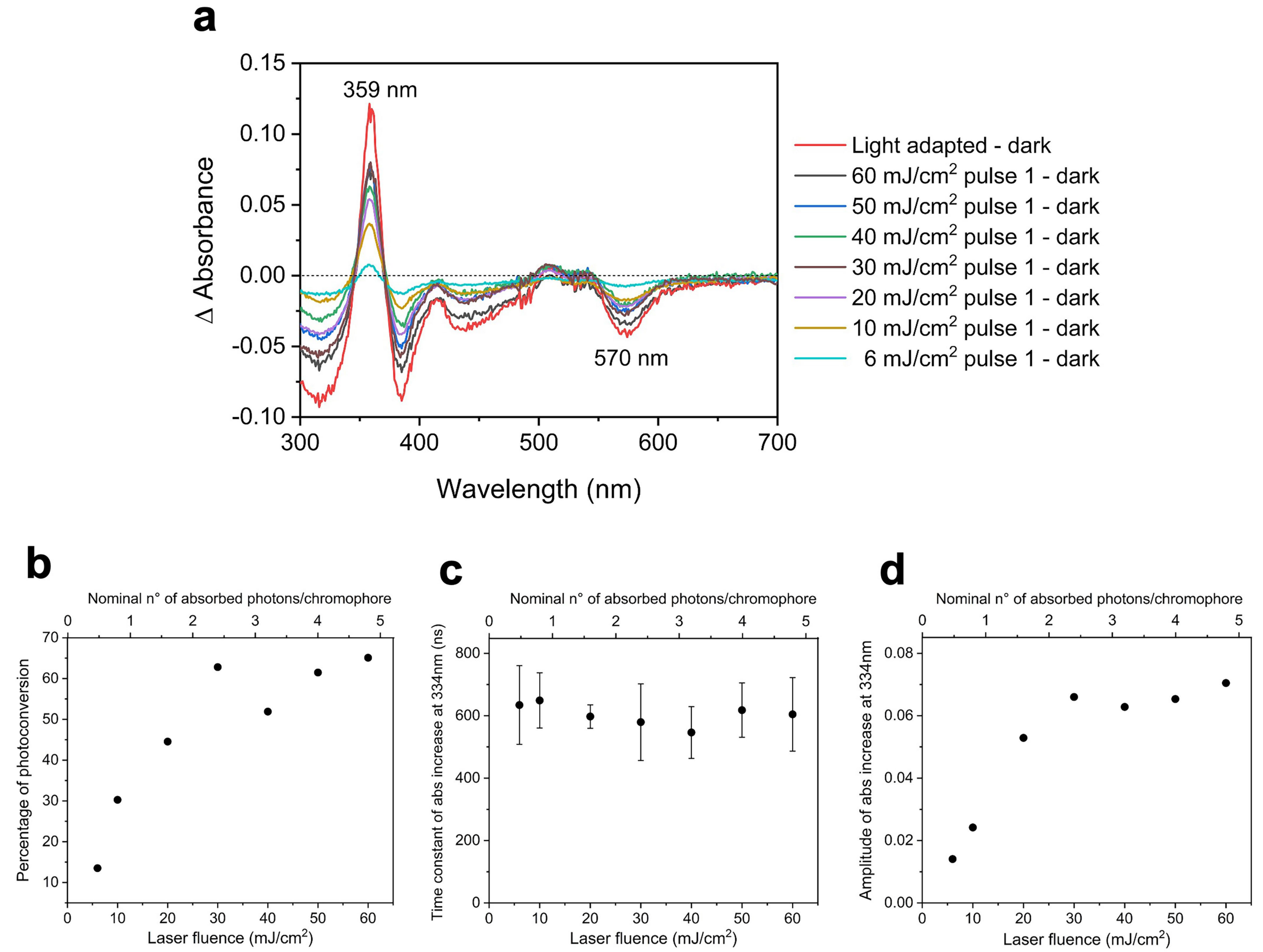

Extended Data Fig. 3 | Spectroscopic pump-laser power titration of photoconversion in *Tt*CBD microcrystals and in solution. (**a**) Absorbance difference spectra of *Tt*CBD microcrystals in CMC before and after excitation with a single ns laser pulse of varying laser fluence at 530 nm from 6 to 60 mJ/cm^2. The non-illuminated sample was used as blank. (**b**) The amount of light state formed in *Tt*CBD microcrystals in CMC as a function of laser fluence (converted to the corresponding number of absorbed photons per chromophore). The amount of light-adapted state was determined by measuring the absorbance at 359 nm, which is characteristic of the bis-histidine light-adapted state. The fully converted light-adapted state was measured by illuminating a *Tt*CBD microcrystalline sample for 2 min with a 530 nm LED. (**c**) The measured time constant for the formation of intermediate 2 (species *iii* in Fig. 1), as determined by monitoring the absorbance change at 334 nm upon excitation with a laser pulse at 530 nm, of *Tt*CBD in solution as a function of laser fluence. The values correspond to the average of five different measurements. Error bars correspond to the standard deviation. (**d**) The amplitude of the absorbance change at 334 nm upon excitation with a laser pulse at 530 nm of *Tt*CBD in solution as a function of laser fluence.

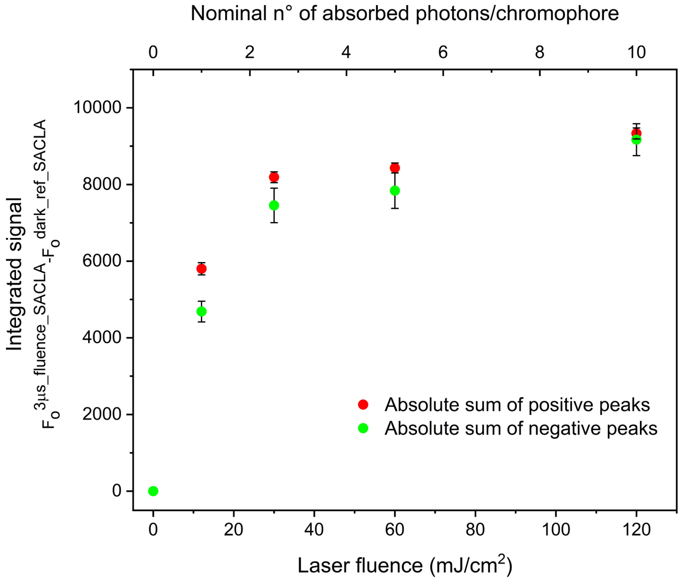

Extended Data Fig. 4 | Crystallographic pump-laser power titration using the light-induced difference signal at 3 µs time delay. Absolute sum of positive (>3σ, green) and negative (<−3σ, red) integrated peaks in the Fourier difference maps calculated between light and dark data sets ($F_o^{3\mu s\_fluence\_SACLA}$ - $F_o^{dark\_ref\_SACLA}$, fluence: 12, 30, 60 and 120 mJ/cm^2) and located within 2 Å from the AdoCbl chromophore was computed and plotted as a function of pump-laser fluence. Data points are the average obtained from 100 Fourier difference maps generated using the bootstrapping method (see Supplementary Methods). Error bars correspond to the standard deviation.

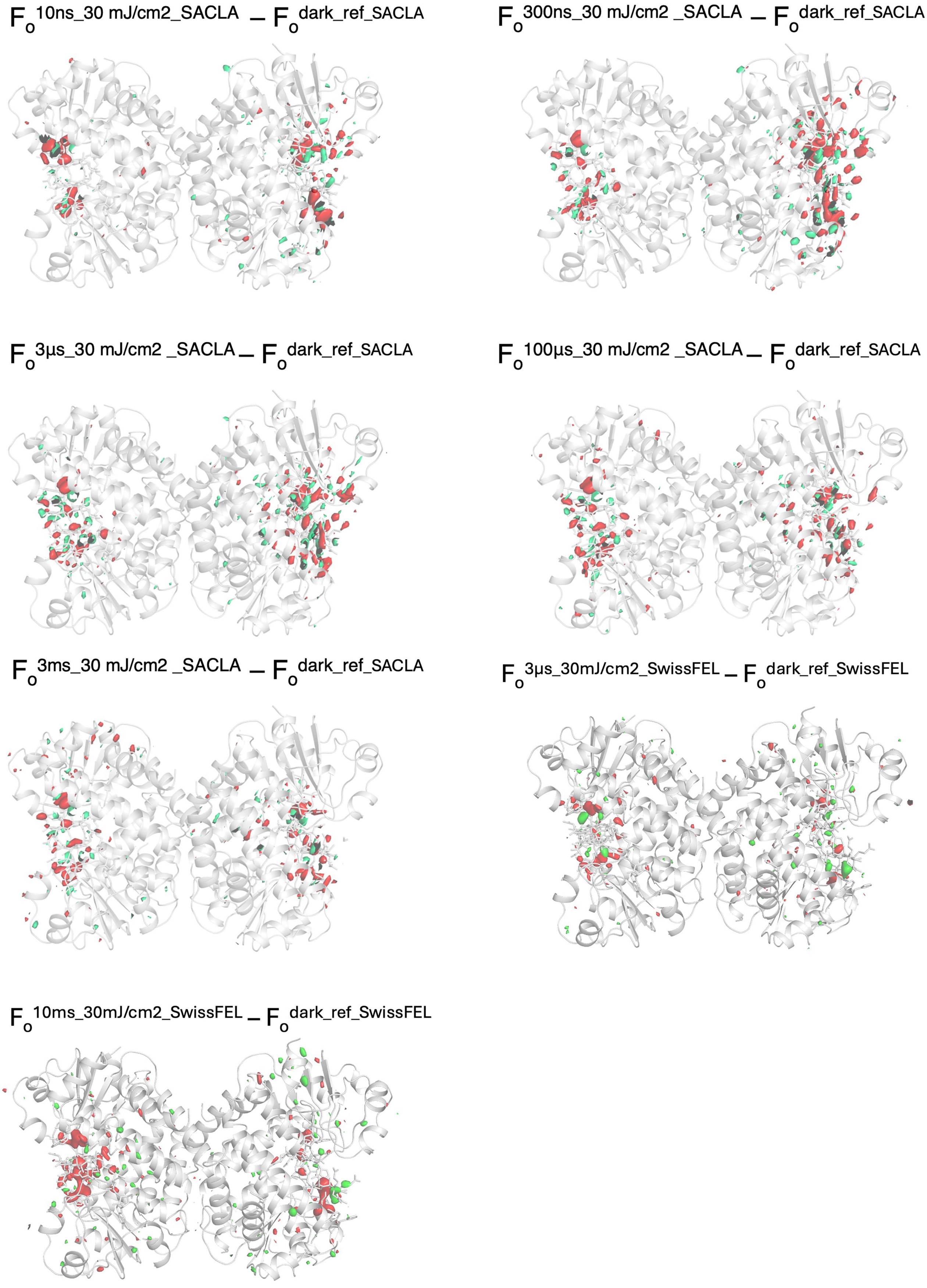

$F_o^{\text{10ns\_30 mJ/cm2\_SACLA}} - F_o^{\text{dark\_ref\_SACLA}}$

$F_o^{\text{300ns\_30 mJ/cm2 \_SACLA}} - F_o^{\text{dark\_ref\_SACLA}}$

$F_o^{\text{3µs\_30 mJ/cm2 \_SACLA}} - F_o^{\text{dark\_ref\_SACLA}}$

$F_o^{\text{100µs\_30 mJ/cm2 \_SACLA}} - F_o^{\text{dark\_ref\_SACLA}}$

$F_o^{\text{3ms\_30 mJ/cm2 \_SACLA}} - F_o^{\text{dark\_ref\_SACLA}}$

$F_o^{\text{3µs\_30mJ/cm2\_SwissFEL}} - F_o^{\text{dark\_ref\_SwissFEL}}$

$F_o^{\text{10ms\_30mJ/cm2\_SwissFEL}} - F_o^{\text{dark\_ref\_SwissFEL}}$

Extended Data Fig. 5 | Overall view of Fourier difference maps from the time series collected at SACLA and SwissFEL. Models of *dark_ref Tt*CBD tetramer (*dark_ref_SACLA* or *dark_ref_SwissFEL*) are represented as a grey cartoon. Fourier difference maps $F_o^{\Delta\text{t\_30mJ/cm2\_SACLA}} - F_o^{\text{dark\_ref\_SACLA}}$ (**Δt**: 10 ns, 300 ns, 3 µs, 100 µs, 3 ms) and $F_o^{\Delta\text{t\_30mJ/cm2\_SwissFEL}} - F_o^{\text{dark\_ref\_SwissFEL}}$ (**Δt**: 3 µs, 10 ms) are contoured at +3.5 (green) and −3.5 σ (red).

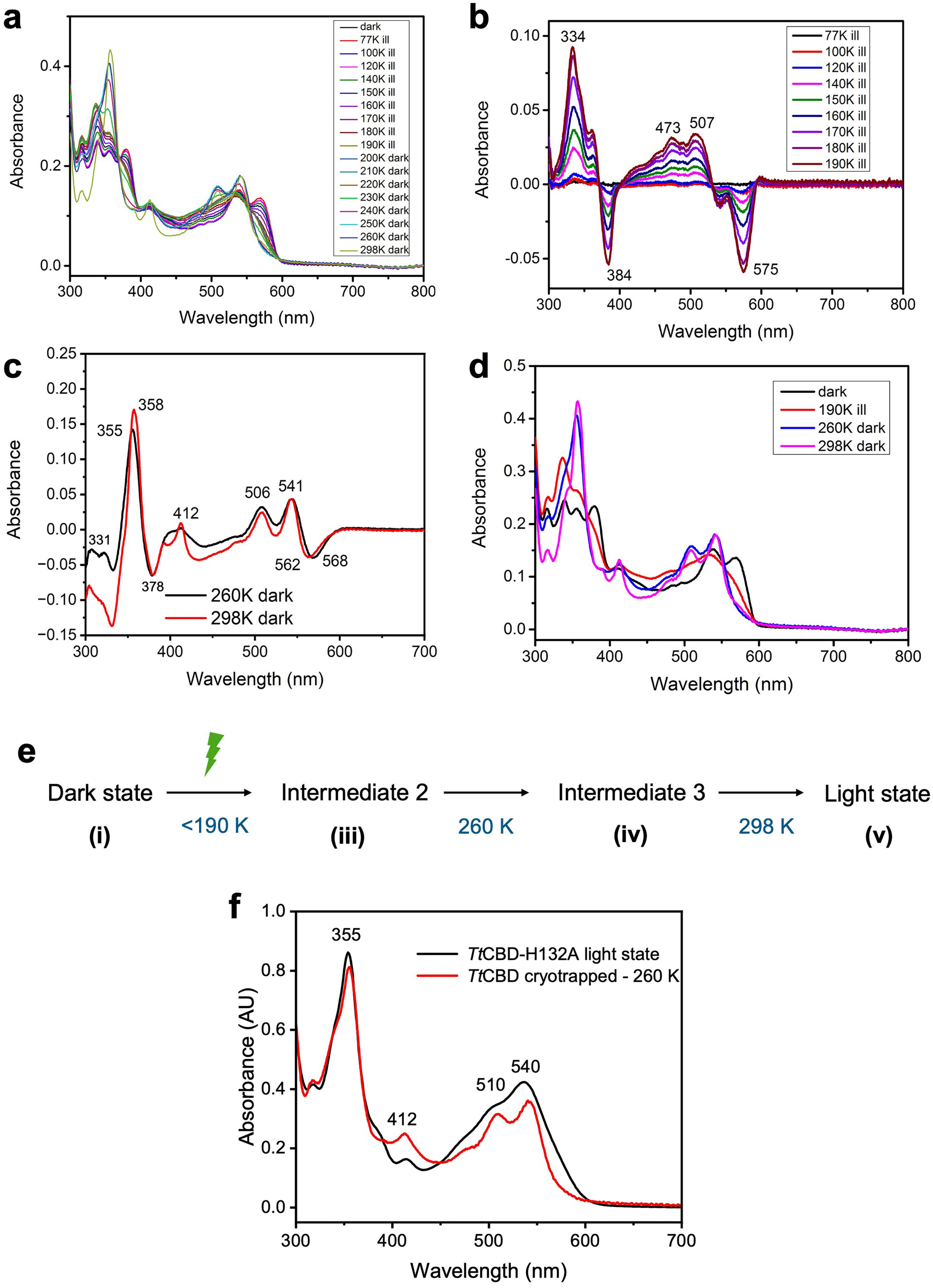

Extended data Fig. 6 | See next page for caption.

Extended data Fig. 6 | Cryotrapping of intermediate states in the photochemical reaction of *Tt*CBD in solution as monitored by temperature-resolved absorption spectroscopy measurements. (**a**) 77 K absorbance spectra of *Tt*CBD in solution (50 μM) after illumination (530 nm) for 15 min at different temperatures ranging from 77 K to 190 K (77 K ill, 100 K ill, etc) or after illumination at 190 K for 15 min and incubation in the dark for 15 min at increasing temperatures (200 K dark, 210 K dark, etc). (**b**) Difference spectra after successive 15 min illumination at increasing temperatures from 77 to 190 K. The non-illuminated sample was used as a baseline. (**c**) Difference spectra after illumination at 190 K for 15 min and incubation in the dark for 15 min at either 260 or 298 K. (**d**) 77 K absorbance spectra of the dark, light (298 K dark) and intermediate states (190 K and 260 K) identified by cryogenic absorbance measurements at 77 K. The wavelengths of the main spectral changes are labelled accordingly in panels **b** and **c**. (**e**) The temperature-resolved absorption spectroscopy data yield the reaction scheme shown here, indicating the temperatures at which each of the intermediate states is formed. The i, iii, iv and v labels illustrate how these species relate to those depicted in Fig. 1 of the main text. (**f**) Spectroscopic intermediate measured at 77 K after illumination (530 nm) at 190 K for 15 min and incubation in the dark for 15 min at 260 K (red curve) and spectrum of the *Tt*CBD-H132A mutant light state measured at room temperature after illumination (530 nm) until complete photoconversion (black curve).

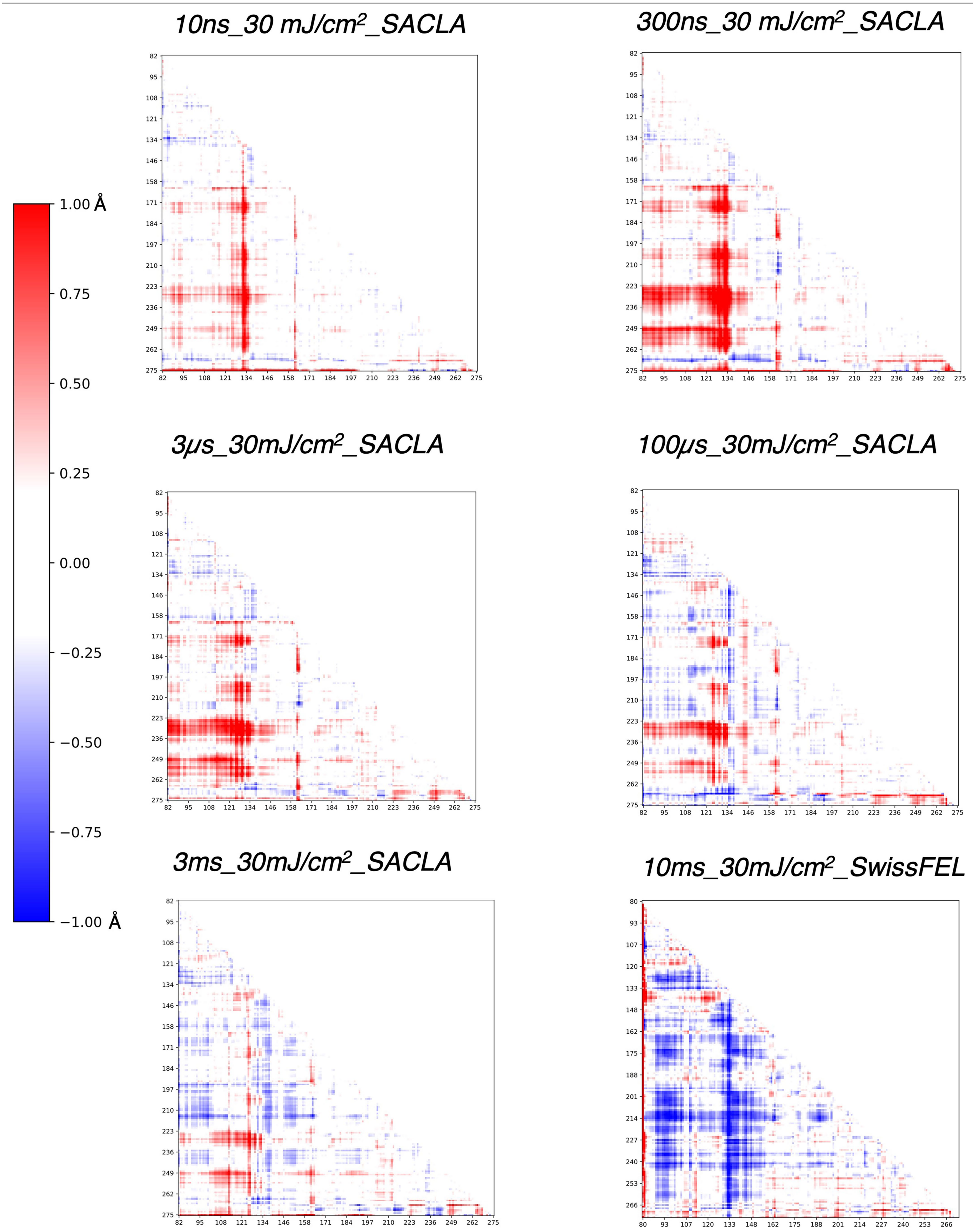

10ns_30 mJ/cm²_SACLA

300ns_30 mJ/cm²_SACLA

3μs_30mJ/cm²_SACLA

100μs_30mJ/cm²_SACLA

3ms_30mJ/cm²_SACLA

10ms_30mJ/cm²_SwissFEL

Extended Data Fig. 7 | Intrachain distance difference matrices (DDM) of monomer B at 10 ns, 300 ns, 3 μs, 100 μs, 3 ms, and 10 ms. DDMs were calculated using *dark_ref_SACLA* model as the reference model from 10 ns to 3 ms and *dark_ref_SwissFEL* model for 10 ms.

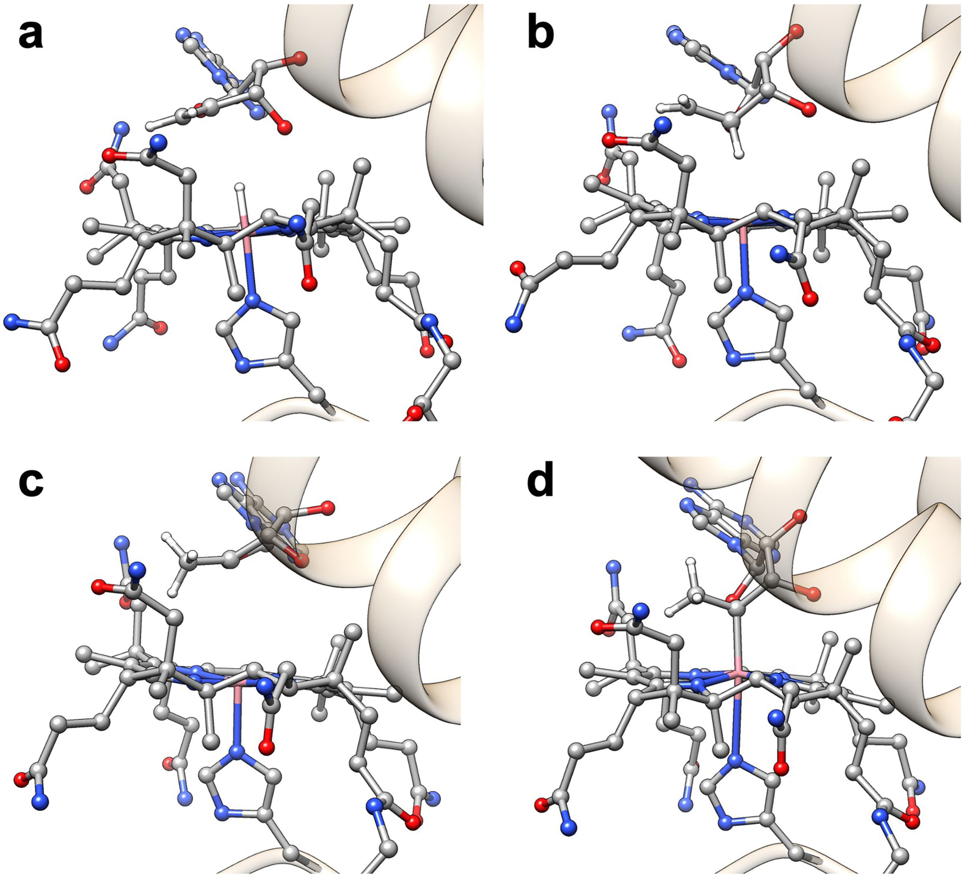

Extended Data Fig. 8 | QM/MM optimised models of *3μs_30mJ/cm^2_SACLA*. QM/MM models generated from the 3 μs crystal structure where four possible scenarios are optimised including (**a**) the photoproducts, (**b**) a primary diradical species where the Co(II)/C5′• radical pair (RP) is formed, (**c**) a tertiary diradical species where the Co(II)/C4′• RP is formed, and (**d**) a stable Co–C4′ adduct.

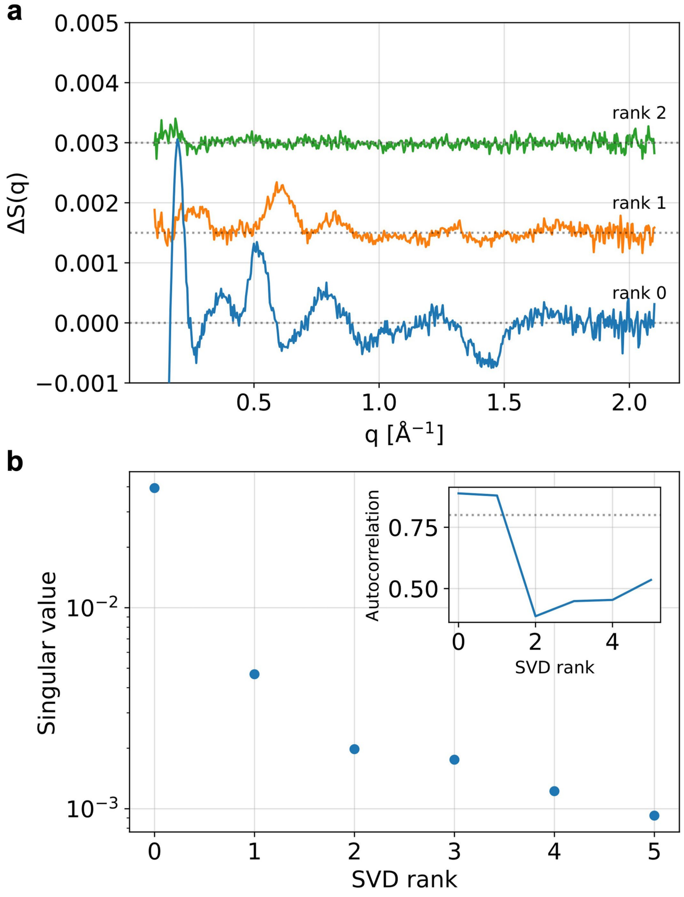

Extended Data Fig. 9 | SVD analysis of TR-XSS data in the 30 µs – 100 ms time range. (**a**) First three SVD basis patterns (left singular vectors) (rank 0 - blue, rank 1 - orange, rank 2 - green). (**b**) The singular values are plotted with blue dots as a function of the rank. The inset shows the autocorrelation of the basis patterns as a function of the rank. A grey dotted line indicates an autocorrelation of 0.8. SVD analysis shows that only two basis patterns contain a signal out of noise.

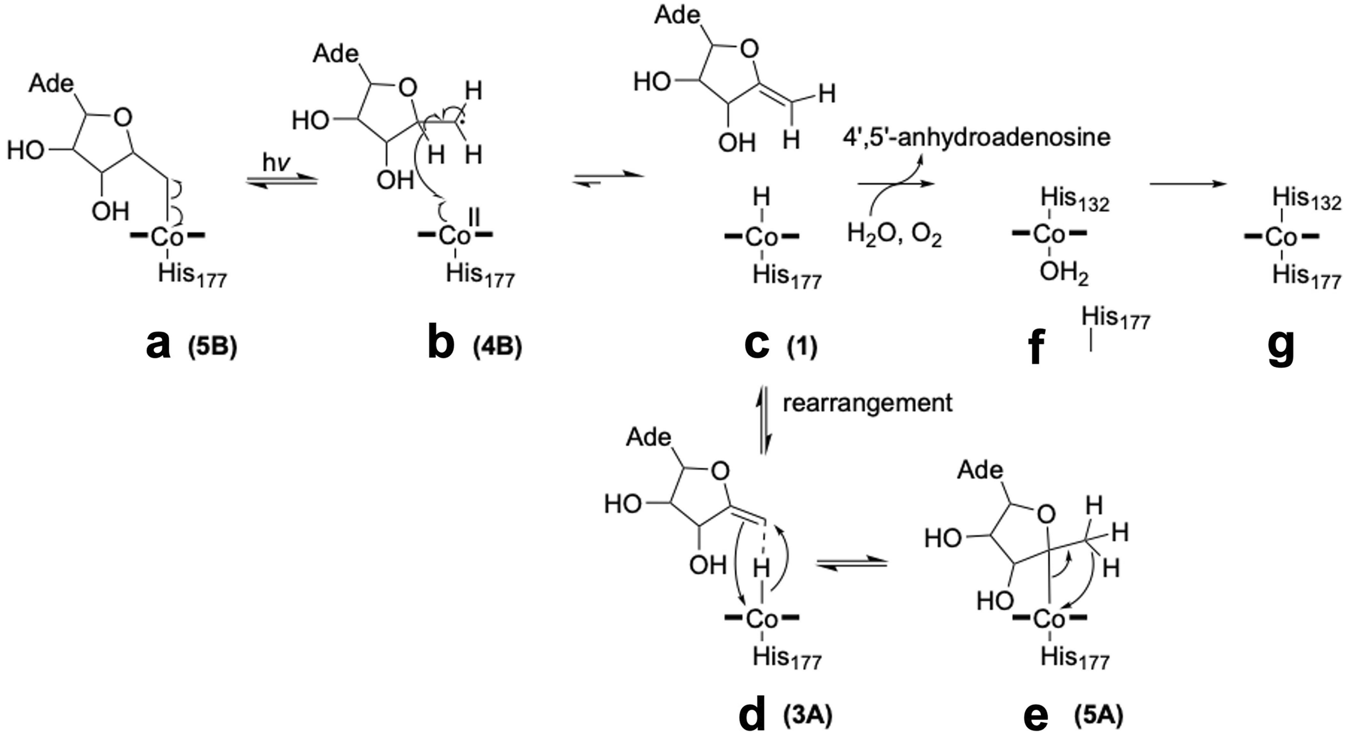

Extended Data Fig. 10 | Proposed CarH photoactivation mechanism based on DFT cluster model calculations. Shown is homolytic photolysis from the dark state (**a**), to a diradical (**b**) followed by formation of the photoproduct (**c**), which can lead to the reversible formation of the Co–C4′ adduct (**e**), via an undetected intermediate species (**d**), or the release of the photoproduct (4′,5′-anhydroadenosine)[20], which leads to the formation of a water-ligated Co(III) species (**f**) and the final light-adapted state[5] (**g**). Names in parentheses refer to the corresponding structures (where appropriate) from Supplementary Fig. 9 and Supplementary Tables 3 and 10. The adenine (Ade) moiety of the 5′-deoxyadenosyl group was omitted for clarity.

nature portfolio

Corresponding author(s): Martin Weik

Last updated by author(s): 2025.08.05

Reporting Summary

Nature Portfolio wishes to improve the reproducibility of the work that we publish. This form provides structure for consistency and transparency in reporting. For further information on Nature Portfolio policies, see our Editorial Policies and the Editorial Policy Checklist.

Statistics

For all statistical analyses, confirm that the following items are present in the figure legend, table legend, main text, or Methods section.

n/a | Confirmed

☐ ☒ The exact sample size (*n*) for each experimental group/condition, given as a discrete number and unit of measurement

☐ ☒ A statement on whether measurements were taken from distinct samples or whether the same sample was measured repeatedly

☒ ☐ The statistical test(s) used AND whether they are one- or two-sided
Only common tests should be described solely by name; describe more complex techniques in the Methods section.

☒ ☐ A description of all covariates tested

☒ ☐ A description of any assumptions or corrections, such as tests of normality and adjustment for multiple comparisons

☐ ☒ A full description of the statistical parameters including central tendency (e.g. means) or other basic estimates (e.g. regression coefficient) AND variation (e.g. standard deviation) or associated estimates of uncertainty (e.g. confidence intervals)

☒ ☐ For null hypothesis testing, the test statistic (e.g. *F*, *t*, *r*) with confidence intervals, effect sizes, degrees of freedom and *P* value noted
Give P values as exact values whenever suitable.

☒ ☐ For Bayesian analysis, information on the choice of priors and Markov chain Monte Carlo settings

☒ ☐ For hierarchical and complex designs, identification of the appropriate level for tests and full reporting of outcomes

☒ ☐ Estimates of effect sizes (e.g. Cohen's *d*, Pearson's *r*), indicating how they were calculated

Our web collection on statistics for biologists contains articles on many of the points above.

Software and code

Policy information about availability of computer code

Data collection	Data collection was performed at multiple facilities. Time-resolved crystallographic data were collected at the SwissFEL using the Cristallina experimental station, and at SACLA using beamline BL2-EH3. Time-resolved solution scattering was conducted at the ESRF on beamline ID09. Macromolecular crystallography data were collected at the ESRF using beamline BM07-FIP2, while serial crystallography data were acquired at the Diamond Light Source on beamline I24. Each facility provided in-house data collection software, which were used during the respective experiments.
Data analysis	X-ray crystallography: CrystFEL (0.10.1 and 0.10.2), DIALS (3.22.1), XDS (Version June 30, 2023), PHASER (2.8), COOT (v 0.9.8.96) CCP4 (8.0.017), Phenix (1.19.2-4158), Xtrapol8 (1.0.0), RADDOSE-3D (v5), PyMOL (3.161), bootstrapping script at https://github.com/coquellen/Bootstrapping. TR-XSS: CRYSOL (3.0), txs (0.0.1) package. Quantum chemistry: Gaussian09, Gaussian16rev. EPR: EasySpin toolbox (5.2.36), Matlab (MATLAB_R2022a). Mass spectrometry: Thermo Scientific Foundation Software v3.0 (Xcalibur). NMR: MestReNova v14.3 (Mestrelab Research). All references are included in the Supplementary Methods section.

For manuscripts utilizing custom algorithms or software that are central to the research but not yet described in published literature, software must be made available to editors and reviewers. We strongly encourage code deposition in a community repository (e.g. GitHub). See the Nature Portfolio guidelines for submitting code & software for further information.

Data

Policy information about availability of data

All manuscripts must include a data availability statement. This statement should provide the following information, where applicable:

- Accession codes, unique identifiers, or web links for publicly available datasets
- A description of any restrictions on data availability
- For clinical datasets or third party data, please ensure that the statement adheres to our policy

Crystal structures have been deposited at the Protein Data Bank (PDB), accession codes: 9S0A, 9S0B, 9S0C, 9S0D, 9S0E, 9S0F, 9S0G, 9S0H, 9S0I, 9S0J, 9S06, 9S07, 9S08, 9S09. All indexed raw images, as well as CrystFEL stream files and merged mtz files for each SFX dataset of this study have been deposited in the Coherent X-ray Imaging Data Bank website (CXIDB) with accession ID 237 (https://dx.doi.org/10.11577/2999572). For all time-resolved datasets, the Fourier difference maps computed with their respective reference datasets have also been deposited (https://dx.doi.org/10.11577/2999572). The CXIDB nomenclature for the different datasets corresponds to the one used in Supplementary Tables 4-6. The TR-XSS data (https://doi.esrf.fr/10.15151/ESRF-ES-704502367 and https://doi.esrf.fr/10.15151/ESRF-ES-1437867878) and cryo-MX data (https://doi.esrf.fr/10.15151/ESRF-DC-2303883862) are available as raw acquisition data from the ESRF WEB site.

Research involving human participants, their data, or biological material

Policy information about studies with human participants or human data. See also policy information about sex, gender (identity/presentation), and sexual orientation and race, ethnicity and racism.

Reporting on sex and gender	N/A
Reporting on race, ethnicity, or other socially relevant groupings	N/A
Population characteristics	N/A
Recruitment	N/A
Ethics oversight	N/A

Note that full information on the approval of the study protocol must also be provided in the manuscript.

Field-specific reporting

Please select the one below that is the best fit for your research. If you are not sure, read the appropriate sections before making your selection.

☒ Life sciences ☐ Behavioural & social sciences ☐ Ecological, evolutionary & environmental sciences

For a reference copy of the document with all sections, see nature.com/documents/nr-reporting-summary-flat.pdf

Life sciences study design

All studies must disclose on these points even when the disclosure is negative.

Sample size	The number of collected and indexed images in TR-SFX experiments necessary to obtain statistically meaningful data has been judged according to the CC1/2 value. For all other experiments, the sample size has been determined based on the SNR.
Data exclusions	No data were excluded from the analyses
Replication	TR-SFX datasets at 3 us were collected at both SACLA (3us_30mJ/cm2_SACLA) and SwissFEL (3us_30mJ/cm2_SwissFEL) facilities. All other SFX time points have not been repeated, as is common practice in the field (scarcity of XFEL beamtime). All experiments other than SFX have been repeated several times and only the results from a single experiments are shown.
Randomization	Randomization is not commonly done in structural biology experiments.
Blinding	Blinding is not commonly done in structural biology experiments.

Reporting for specific materials, systems and methods

We require information from authors about some types of materials, experimental systems and methods used in many studies. Here, indicate whether each material, system or method listed is relevant to your study. If you are not sure if a list item applies to your research, read the appropriate section before selecting a response.

Materials & experimental systems

n/a	Involved in the study
☒	☐ Antibodies
☒	☐ Eukaryotic cell lines
☒	☐ Palaeontology and archaeology
☒	☐ Animals and other organisms
☒	☐ Clinical data
☒	☐ Dual use research of concern
☒	☐ Plants

Methods

n/a	Involved in the study
☒	☐ ChIP-seq
☒	☐ Flow cytometry
☒	☐ MRI-based neuroimaging

Plants

Seed stocks	N/A
Novel plant genotypes	N/A
Authentication	N/A